

# 3D Wideband Non-Stationary Geometry-Based Stochastic Models for Non-Isotropic MIMO Vehicle-to-Vehicle Channels

Yi Yuan, Cheng-Xiang Wang, *Senior Member, IEEE*, Yejun He, *Senior Member, IEEE*, Mohammed M. Alwakeel, *Senior Member, IEEE*, and el-Hadi M. Aggoune, *Senior Member, IEEE*

**Abstract**—Actual vehicle-to-vehicle (V2V) channel measurements have shown that the wide-sense stationary (WSS) modeling assumption is valid only for very short time intervals. This fact motivates us to develop non-WSS V2V channel models. In this paper, we propose a novel three-dimensional (3D) theoretical non-WSS regular-shaped geometry-based stochastic model (RS-GBSM) and the corresponding sum-of-sinusoids (SoS) simulation model for non-isotropic scattering wideband multiple-input multiple-output (MIMO) V2V fading channels. The movements of the transmitter (Tx), scatterers, and receiver (Rx) result in the time-varying angles of departure (AoDs) and angles of arrival (AoAs) that make our models non-stationary. The proposed RS-GBSMs, combining line-of-sight (LoS) components, a two-sphere model, and multiple confocal elliptic-cylinder models, have the ability to study the impacts of vehicular traffic density (VTD) and non-stationarity on channel statistics, and jointly consider the azimuth and elevation angles by using the von Mises Fisher (VMF) distribution. The proposed RS-GBSMs are sufficiently generic and adaptable to model various V2V scenarios. Based on the proposed 3D non-WSS RS-GBSMs, important local channel statistical properties are derived and thoroughly investigated. The impacts of VTD and non-stationarity on these channel statistical properties are investigated by comparing them with those of the corresponding WSS model. The proposed non-WSS RS-GBSMs are validated by measure-

ments in terms of the channel stationary time. Finally, numerical and simulation results demonstrate that the 3D non-WSS model is more practical to characterize real V2V channels.

**Index Terms**—Vehicle-to-vehicle wideband channels, non-stationary, 3D MIMO channel models, non-isotropic, local statistical properties.

## I. INTRODUCTION

VEHICLE-TO-VEHICLE (V2V) communications play a substantial role in practical applications of inter-vehicle ad hoc networks [1], such as emergency management [2], cooperative communications [3], [4], mobile infotainment, and dedicated short-range communications (DSRC) for intelligent transportation systems (IEEE 802.11p) [5]. For the development of V2V communication systems, the knowledge of underlying propagation channels is required. Channel modeling is an effective solution to investigate the real physical attenuation by reliably describing the channel characteristics [6]–[8]. In addition, the advantages of multiple-input multiple-output (MIMO) technology can satisfy the growing demands for high data transmission and enhance link reliability by efficiently exploiting multipath propagation [9].

In V2V communication systems, both the transmitter (Tx) and receiver (Rx) are in motion and equipped with low elevation antennas. The feature of high mobility in vehicular environment makes conventional cellular fixed-to-mobile (F2M) channel models no longer applicable to V2V channels, especially considering the Doppler effect on both the Tx and Rx. Therefore, the modeling of real V2V fading channels has been receiving more and more attention, such as [10]–[32].

In [10], we have proposed a novel three-dimensional (3D) narrowband MIMO V2V RS-GBSM for non-isotropic scattering Ricean fading channels. However, most potential transmission schemes for V2V communications use relatively wide bandwidths (e.g., 75 MHz for the IEEE 802.11p standard [5]). The underlying V2V channels present frequency-selectivity since the signal bandwidth is larger than or in the order of the coherence bandwidth (normally 4–6 MHz [11]). Therefore, wideband V2V channel models are indispensable.

Most V2V channel models in the literature rely on the wide-sense stationary (WSS) assumption. These WSS V2V channel models can be classified as geometry-based deterministic models (GBDMs) [31] and stochastic models, which can be further categorized as non-geometry-based stochastic models (NGSMs) [32] and geometry-based stochastic models

Manuscript received April 14, 2014; revised January 28, 2015 and April 29, 2015; accepted July 5, 2015. Date of publication July 28, 2015; date of current version December 8, 2015. This work was supported by SNCS Research Center, University of Tabuk, Ministry of Higher Education in Saudi Arabia, the EU FP7 QUICK project (No. PIRSES-GA-2013-612652), the EU H2020 ITN 5G Wireless project (No. 641985), the 863 project in 5G, Ministry of Science and Technology in China (No. 2014AA01A707), the Fundamental Research Program of Shenzhen City (No. JCYJ20120817163755061 and JC201005250067A), and National Natural Science Foundation of China (No. 61101079 and 61372077). The associate editor coordinating the review of this paper and approving it for publication was F. Falcone.

Y. Yuan is with the Institute of Sensors, Signals and Systems, School of Engineering & Physical Sciences, Heriot-Watt University, Edinburgh EH14 4AS, U.K., and also with the SNCS Research Center, University of Tabuk, Tabuk 71491, Saudi Arabia (e-mail: yyuan1116@gmail.com).

C.-X. Wang is with the Institute of Sensors, Signals and Systems, School of Engineering & Physical Sciences, Heriot-Watt University, Edinburgh EH14 4AS, U.K., with the School of Information Science and Engineering, Shandong University, Jinan 250100, China, and also with the SNCS Research Center, University of Tabuk, Tabuk 71491, Saudi Arabia (e-mail: cheng-xiang.wang@hw.ac.uk).

Y. He is with College of Information Engineering, Shenzhen University, Shenzhen 518160, China (e-mail: heyejun@ieec.org).

M. M. Alwakeel and e. M. Aggoune are with the SNCS Research Center, University of Tabuk, Tabuk 71491, Saudi Arabia (e-mail: alwakeel@ut.edu.sa; haggoune.snscs@ut.edu.sa).

Color versions of one or more of the figures in this paper are available online at <http://ieeexplore.ieee.org>.

Digital Object Identifier 10.1109/TWC.2015.2461679

(GBSMs) [12]–[22]. Furthermore, GBSMs can be classified as regular-shaped GBSMs (RS-GBSMs) [13]–[21] and irregular-shaped GBSMs (IS-GBSMs) [22], [23], depending on whether effective scatterers are located on regular shapes, e.g., one-ring, two-ring, ellipses, or irregular shapes.

The aforementioned WSS V2V channel models [12]–[23] assumed that channel statistics are unchanged with respect to time. However, measurement results for V2V channels in [22]–[25] have shown that the WSS assumption is valid only for very short time intervals (in the order of millisecond [24]). The growth of V2V channel measurements has forced researchers to re-evaluate the validity of the WSS conditions. This fact motivates us to develop non-stationary channel models. However, only few channel models [26]–[30] take into account the non-stationary behaviour of V2V channels. In [33], the author first introduced the concept of the local scattering function (LSF) to describe the channel non-stationarity. The generalized non-WSS narrowband MIMO V2V channel model has been characterized in [26]. The model has been further extended to wideband case in [27]. In [28] and [29], authors proposed two-dimensional (2D) geometry-based non-WSS narrowband MIMO V2V channel models for straight road and T-junction scenarios, respectively. In [30], the impact of the channel non-stationarity on V2V channel capacity is addressed.

The 3D RS-GBSMs in [10] have been proved that the 3D scattering should be considered for realistic V2V channel modeling. In this paper, we further extend the models proposed in [10] to wideband and fulfil the requirement of non-stationary channel models. The angle of departure (AoD) and the angle of arrival (AoA) are supposed to be time-variant, which makes our channel model non-stationary. Besides that, V2V channel measurements in [11] have proved that the total number of taps also has the non-stationary feature. The death/birth process can be applied to describe the time-varying number of the taps.

The proposed theoretical 3D RS-GBSM is the combination of line-of-sight (LoS) components, a two-sphere model, and multiple confocal elliptic-cylinder models with single- and double-bounced rays, for non-isotropic MIMO V2V channels, which is sufficiently generic and adaptable to model various non-stationary V2V channels for different scenarios. It is also the first 3D non-WSS RS-GBSM that has the ability to study the impact of the vehicle traffic density (VTD) on channel statistics, and jointly considers the azimuth and elevation angles by applying the von Mises-Fisher (VMF) distribution as the scatterer distribution. The 3D theoretical RS-GBSM assumes infinite numbers of effective scatterers, which results in an infinite complexity. Therefore, it cannot be implemented in practice. Hence, this paper develops the corresponding 3D MIMO V2V sum-of-sinusoids (SoS) based simulation model with the 3D parameter computation method proposed in [10].

Overall, the major contributions and novelties of this paper are summarized as follows:

- 1) Based on our previous work in [10], the extension for wideband and non-WSS RS-GBSM is proposed with time-varying parameters. The V2V channel model considers the impact of both moving and fixed scatterers on channel statistics.

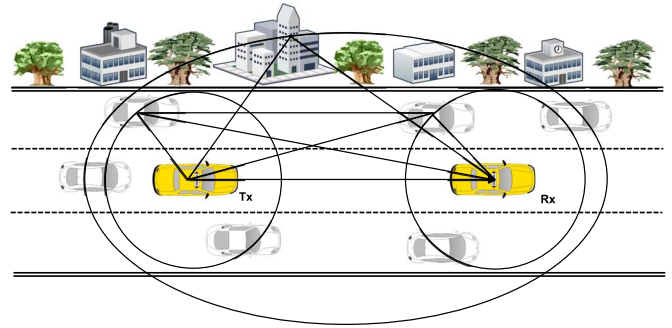


Fig. 1. The typical V2V communication including moving and static scatterers with LoS, single- and double-bounced rays.

- 2) To better understand the non-stationary channel behavior, important channel local statistical properties are derived and thoroughly investigated, i.e., space-time (ST) correlation function (CF), frequency correlation function (FCF), and power delay profile (PDP).
- 3) The corresponding SoS simulation model is developed by the 3D parameter computation method, namely the method of equal volume (MEV), which is able to jointly calculate the azimuth and elevation angles.
- 4) The impacts of the non-stationarity and VTD on ST CF are investigated by comparing with those of the corresponding WSS model.
- 5) The ST CF of our SoS simulation model is verified by comparing it with that of the reference model and simulated results. The results show that the simulation model is an excellent approximation of the reference model.
- 6) The proposed non-WSS RS-GBSMs are validated by measurements in [24] according to the stationary time.

The proposed models and our research findings on channel local statistical properties can be applied to link and system level simulations, such as multiple-antenna capacity studies [37], [38], co-channel interference on MIMO networks [39], vehicle location and navigation systems [40], and IEEE 802.11p system [5].

The rest of this paper is organized as follows. In Section II, the proposed theoretical 3D non-WSS wideband MIMO V2V channel model is developed by considering the time-varying parameters. Section III presents the local statistical properties of the 3D V2V channel model. In Section IV, the corresponding 3D SoS simulation model is briefly introduced with the 3D parameter computation method. Numerical simulation results and analysis are presented in Section V. Finally, the conclusions are drawn in Section VI.

## II. 3D WIDEBAND NON-STATIONARY MIMO V2V THEORETICAL CHANNEL MODELS

Fig. 1 shows a typical V2V communication scenario with LoS, single- and double-bounced rays. The proposed generic wideband model employs a RS-GBSM approach to represent the multipath propagation channel between a Tx and a Rx. Let us now consider a 3D wideband MIMO V2V communication system with  $M_T$  transmit and  $M_R$  receive omni-directional antenna elements. Both the Tx and Rx are equipped with low elevation antennas. The MIMO fading channel can be described by a

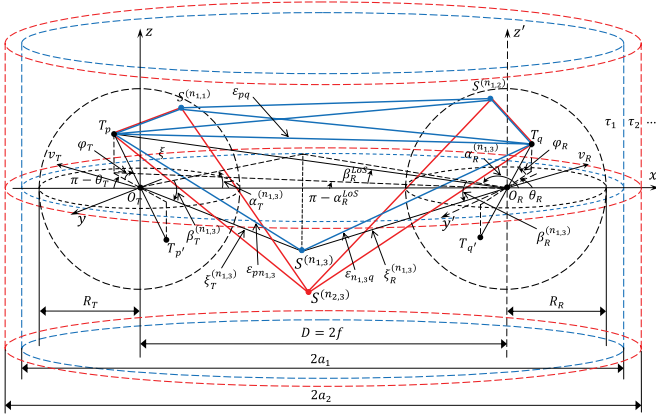


Fig. 2. The proposed 3D RS-GBSM combining two-sphere model and multiple confocal elliptic-cylinder models with LoS, single- and double-bounced rays for a wideband MIMO V2V channel (Blue solid line: tap 1; Red solid line: tap 2) (only showing the detailed geometry of LoS components and single-bounced rays in the first tap elliptic-cylinder model).

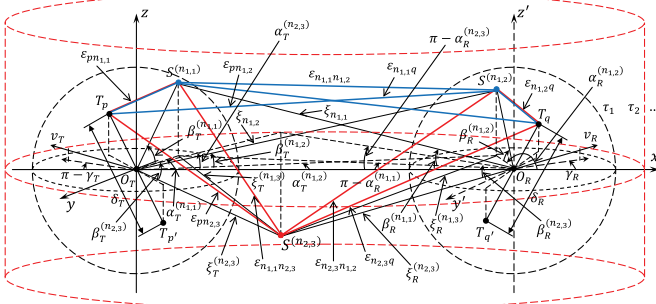


Fig. 3. The detailed geometry of the single- and double-bounced rays in the two-sphere model and single-bounced rays in the second tap elliptic-cylinder model (Blue solid line: tap 1; Red solid line: tap 2).

matrix  $\mathbf{H}(t) = [h_{pq}(t, \tau')]_{M_R \times M_T}$  of size  $M_R \times M_T$ . Figs. 2 and 3 illustrate the detailed 3D wideband V2V channel model between the Tx and Rx with LoS components, single- and double-bounced scattering. To consider the impact of the VTD on channel statistics, we need to distinguish between the moving vehicles around the Tx and Rx and the stationary roadside environments (e.g., buildings, trees, parked cars, etc.). Therefore, we use the two-sphere model to mimic the moving vehicles and the multiple confocal elliptic-cylinder models to depict the stationary roadside environments as shown in Fig. 1. For better readability purposes, Fig. 2 only shows the geometry of LoS components, and the single-bounced multiple confocal elliptic-cylinder models. The detailed geometry of the single- and double-bounced two-sphere model is given in Fig. 3. According to the tapped delay line (TDL) concept, the complex impulse response between the  $p$ th ( $p = 1, \dots, M_T$ ) antenna of the Tx (i.e.,  $T_p$ ) and the  $q$ th ( $q = 1, \dots, M_R$ ) antenna of the Rx (i.e.,  $T_q$ ) can be expressed as

$$h_{pq}(t, \tau') = \sum_{l=1}^{L(t)} c_l h_{l,pq}(t) \delta(\tau' - \tau'_l) \quad (1)$$

where the subscript  $l$  is the tap number,  $L(t)$  is the total number of taps, and  $c_l$  represents the gain of the  $l$ th tap.  $h_{l,pq}(t)$  and  $\tau'_l$  denote the complex time-variant tap coefficients and the

discrete propagation delay of the  $l$ th tap, respectively. Hence,  $h_{l,pq}(t)$  is a narrowband process.

### A. First Tap

In Fig. 2, we used uniform linear antenna arrays with  $M_T = M_R = 2$  as an example. The two-sphere model defines two spheres of effective scatterers, one around the Tx and the other around the Rx. For the first tap, we suppose that there are  $N_{1,1}$  effective scatterers around the Tx lying on a sphere of radius  $R_T$  and the  $n_{1,1}$ th ( $n_{1,1} = 1, \dots, N_{1,1}$ ) effective scatterer is denoted by  $s^{(n_{1,1})}$ . Similarly, assume there are  $N_{1,2}$  effective scatterers around the Rx lying on a sphere of radius  $R_R$  and the  $n_{1,2}$ th ( $n_{1,2} = 1, \dots, N_{1,2}$ ) effective scatterer is denoted by  $s^{(n_{1,2})}$ .

The multiple confocal elliptic-cylinder models with the Tx and Rx located at the foci represents the TDL structure and have  $N_{l,3}$  effective scatterers on the  $l$ th elliptic-cylinder (i.e.,  $l$ th tap), where  $l = 1, 2, \dots, L(t)$  with  $L(t)$  being the time-varying total number of elliptic-cylinders or taps. The semi-major axis of the  $l$ th elliptic-cylinder and the  $n_{l,3}$ th ( $n_{l,3} = 1, \dots, N_{l,3}$ ) effective scatterer are denoted by  $a_l$  and  $s^{(n_{l,3})}$ , respectively. The distance between the Tx and Rx is  $D = 2f$  with  $f$  denoting the half length of the distance between the two focal points of ellipses. The antenna element spacings at the Tx and Rx are designated by  $\delta_T$  and  $\delta_R$ , respectively. The parameters in Figs. 2 and 3 are defined in Table I. Note that the reasonable assumptions  $D \gg \max\{R_T, R_R\}$  and  $\min\{R_T, R_R, a - f\} \gg \max\{\delta_T, \delta_R\}$  are applied in this theoretical model [16].

From the above 3D RS-GBSM, the complex tap coefficient for the first tap of the  $T_p \rightarrow T_q$  link is a superposition of the LoS, single- and double-bounced components, and can be expressed as

$$h_{1,pq}(t) = h_{1,pq}^{LoS}(t) + \sum_{i=1}^I h_{1,pq}^{SB_i}(t) + h_{1,pq}^{DB}(t) \quad (2)$$

with

$$h_{1,pq}^{LoS}(t) = \sqrt{\frac{K}{K+1}} e^{-j2\pi f_c \tau_{pq}} \times e^{j2\pi f_{T_{max}} t \cos(\alpha_T^{LoS} - \gamma_T) \cos \beta_T^{LoS}} \times e^{j2\pi f_{R_{max}} t \cos(\alpha_R^{LoS} - \gamma_R) \cos \beta_R^{LoS}} \quad (3a)$$

$$h_{1,pq}^{SB_i}(t) = \sqrt{\frac{\eta_{SB_{1,i}}}{K+1}} \lim_{N_{1,1}, N_{1,2} \rightarrow \infty} \sum_{n_{1,1}=1}^{N_{1,1}} \frac{1}{\sqrt{N_{1,1}}} e^{j(\psi_{n_{1,1}} - 2\pi f_c \tau_{pq, n_{1,1}})} \times e^{j2\pi f_{T_{max}} t \cos(\alpha_T^{(n_{1,1})} - \gamma_T) \cos \beta_T^{(n_{1,1})}} \times e^{j2\pi f_{R_{max}} t \cos(\alpha_R^{(n_{1,1})} - \gamma_R) \cos \beta_R^{(n_{1,1})}} \quad (3b)$$

$$h_{1,pq}^{DB}(t) = \sqrt{\frac{\eta_{DB_{1,1}}}{K+1}} \lim_{N_{1,1}, N_{1,2} \rightarrow \infty} \sum_{n_{1,1}, n_{1,2}=1}^{N_{1,1}, N_{1,2}} \frac{1}{\sqrt{N_{1,1} N_{1,2}}} \times e^{j(\psi_{n_{1,1}, n_{1,2}} - 2\pi f_c \tau_{pq, n_{1,1}, n_{1,2}})} \times e^{j2\pi f_{T_{max}} t \cos(\alpha_T^{(n_{1,1})} - \gamma_T) \cos \beta_T^{(n_{1,1})}} \times e^{j2\pi f_{R_{max}} t \cos(\alpha_R^{(n_{1,2})} - \gamma_R) \cos \beta_R^{(n_{1,2})}} \quad (3c)$$

where  $\tau_{pq} = \varepsilon_{pq}/c$ ,  $\tau_{pq, n_{1,1}} = (\varepsilon_{pn_{1,1}} + \varepsilon_{n_{1,1}q})/c$ , and  $\tau_{pq, n_{1,1}, n_{1,2}} = (\varepsilon_{pn_{1,1}} + \varepsilon_{n_{1,1}, n_{1,2}} + \varepsilon_{n_{1,2}q})/c$  are travel times of the waves

TABLE I  
DEFINITION OF PARAMETERS IN FIGS. 2 AND 3

$D$	distance between the centers of the Tx and Rx spheres
$R_T, R_R$	radius of the Tx and Rx spheres, respectively
$a_l, f$	semi-major axis and half spacing between two foci of the elliptic-cylinder, respectively
$\delta_T, \delta_R$	antenna element spacing at the Tx and Rx, respectively
$\theta_T, \theta_R$	orientation of the Tx and Rx antenna array in the $x$ - $y$ plane, respectively
$\varphi_T, \varphi_R$	elevation of the Tx and Rx antenna array relative to the $x$ - $y$ plane, respectively
$v_T, v_R$	velocities of the Tx and Rx, respectively
$\gamma_T, \gamma_R$	moving directions of the Tx and Rx in the $x$ - $y$ plane, respectively
$\alpha_T^{(n_{l,i})}$ ( $i = 1, 2, 3$ ) ( $l = 1, 2, \dots, L(t)$ )	azimuth angle of departure (AAoD) of the waves that impinge on the effective scatterers $s^{(n_{l,i})}$
$\alpha_R^{(n_{l,i})}$ ( $i = 1, 2, 3$ ) ( $l = 1, 2, \dots, L(t)$ )	azimuth angle of arrival (AAoA) of the waves traveling from the effective scatterers $s^{(n_{l,i})}$
$\beta_T^{(n_{l,i})}$ ( $i = 1, 2, 3$ ) ( $l = 1, 2, \dots, L(t)$ )	elevation angle of departure (EAoD) of the waves that impinge on the effective scatterers $s^{(n_{l,i})}$
$\beta_R^{(n_{l,i})}$ ( $i = 1, 2, 3$ ) ( $l = 1, 2, \dots, L(t)$ )	elevation angle of arrival (EAoA) of the waves traveling from the effective scatterers $s^{(n_{l,i})}$
$\alpha_R^{LoS}, \beta_R^{LoS}$	AAoA and EAoA of the LoS paths, respectively
$\varepsilon_{pq}, \varepsilon_{pn_{l,i}}, \varepsilon_{n_{l,1}n_{l,2}}, \varepsilon_{n_{l,i}q}, \xi, \xi_{T(R)}^{n_{l,3}}, \xi_{n_{l,1}}, \xi_{n_{l,2}}$ ( $i = 1, 2, 3$ ) ( $l = 1, 2, \dots, L(t)$ )	distances $d(T_p, T_q)$ , $d(T_p, s^{(n_{l,i})})$ , $d(s^{(n_{l,1})}, s^{(n_{l,2})})$ , $d(s^{(n_{l,i})}, T_q)$ , $d(T_p, O_R)$ , $d(O_T(O_R), s^{(n_{l,3})})$ , $d(s^{(n_{l,1})}, O_R)$ , $d(O_T, s^{(n_{l,2})})$ , respectively

through the link  $T_p \rightarrow T_q$ ,  $T_p \rightarrow s^{(n_{l,i})} \rightarrow T_q$ , and  $T_p \rightarrow s^{(n_{l,1})} \rightarrow s^{(n_{l,2})} \rightarrow T_q$ , respectively, as shown in Figs. 2 and 3. There are three single-bounced components in the first tap, i.e.,  $l = 3$ . The  $c$  and  $K$  designate the speed of light and the Ricean factor, respectively. Energy-related parameters  $\eta_{SB_{l,i}}$  and  $\eta_{DB_{l,1}}$  specify how much the single- and double-bounced rays contribute to the total scattered power of the first tap, respectively. Note that these energy-related parameters are normalized to satisfy  $\sum_{i=1}^l \eta_{SB_{l,i}} + \eta_{DB_{l,1}} = 1$ .

### B. Other Taps

The complex tap coefficient for other taps ( $l > 1$ ) of the  $T_p \rightarrow T_q$  link is a superposition of the single- and double-bounced components, and can be expressed as

$$h_{l,pq}(t) = h_{l,pq}^{SB_3}(t) + h_{l,pq}^{DB_1}(t) + h_{l,pq}^{DB_2}(t) \quad (4)$$

with

$$h_{l,pq}^{SB_3}(t) = \sqrt{\eta_{SB_{l,3}}} \lim_{N_{l,3} \rightarrow \infty} \sum_{n_{l,3}=1}^{N_{l,3}} \frac{1}{\sqrt{N_{l,3}}} e^{j(\psi_{n_{l,3}} - 2\pi f_c \tau_{pq,n_{l,3}})} \times e^{j2\pi f_{T_{max}} t \cos(\alpha_T^{(n_{l,3})} - \gamma_T) \cos \beta_T^{(n_{l,3})}} \times e^{j2\pi f_{R_{max}} t \cos(\alpha_R^{(n_{l,3})} - \gamma_R) \cos \beta_R^{(n_{l,3})}} \quad (5a)$$

$$h_{l,pq}^{DB_1}(t) = \sqrt{\eta_{DB_{l,1}}} \lim_{N_{l,1}, N_{l,3} \rightarrow \infty} \sum_{n_{l,1}, n_{l,3}=1}^{N_{l,1}, N_{l,3}} \frac{1}{\sqrt{N_{l,1} N_{l,3}}} \times e^{j(\psi_{n_{l,1}, n_{l,3}} - 2\pi f_c \tau_{pq,n_{l,1}, n_{l,3}})} \times e^{j2\pi f_{T_{max}} t \cos(\alpha_T^{(n_{l,1})} - \gamma_T) \cos \beta_T^{(n_{l,1})}} \times e^{j2\pi f_{R_{max}} t \cos(\alpha_R^{(n_{l,3})} - \gamma_R) \cos \beta_R^{(n_{l,3})}} \quad (5b)$$

$$h_{l,pq}^{DB_2}(t) = \sqrt{\eta_{DB_{l,2}}} \lim_{N_{l,2}, N_{l,3} \rightarrow \infty} \sum_{n_{l,2}, n_{l,3}=1}^{N_{l,2}, N_{l,3}} \frac{1}{\sqrt{N_{l,2} N_{l,3}}} \times e^{j(\psi_{n_{l,2}, n_{l,3}} - 2\pi f_c \tau_{pq,n_{l,2}, n_{l,3}})} \times e^{j2\pi f_{T_{max}} t \cos(\alpha_T^{(n_{l,2})} - \gamma_T) \cos \beta_T^{(n_{l,2})}} \times e^{j2\pi f_{R_{max}} t \cos(\alpha_R^{(n_{l,3})} - \gamma_R) \cos \beta_R^{(n_{l,3})}} \quad (5c)$$

where  $\tau_{pq,n_{l,3}} = (\varepsilon_{pn_{l,3}} + \varepsilon_{n_{l,3}q})/c$ ,  $\tau_{pq,n_{l,1}, n_{l,3}} = (\varepsilon_{pn_{l,1}} + \varepsilon_{n_{l,1}n_{l,3}} + \varepsilon_{n_{l,3}q})/c$ , and  $\tau_{pq,n_{l,3}, n_{l,2}} = (\varepsilon_{pn_{l,3}} + \varepsilon_{n_{l,3}n_{l,2}} + \varepsilon_{n_{l,2}q})/c$  are travel times of the waves through the link  $T_p \rightarrow s^{(n_{l,3})} \rightarrow T_q$ ,  $T_p \rightarrow s^{(n_{l,1})} \rightarrow s^{(n_{l,3})} \rightarrow T_q$ , and  $T_p \rightarrow s^{(n_{l,3})} \rightarrow s^{(n_{l,2})} \rightarrow T_q$ , respectively, as illustrated in Figs. 2 and 3. Again, energy-related parameters  $\eta_{SB_{l,3}}$  and  $\eta_{DB_{l,1(2)}}$  specify how much the single- and double-bounced rays contribute to the total scattered power of other taps, respectively. Note that these energy-related parameters also satisfy  $\eta_{SB_{l,3}} + \eta_{DB_{l,1}} + \eta_{DB_{l,2}} = 1$ . The phases  $\psi_{n_{l,i}}$ ,  $\psi_{n_{l,1}, n_{l,2}}$ ,  $\psi_{n_{l,3}}$ , and  $\psi_{n_{l,1(2)}, n_{l,3}}$  are independent and identically distributed (i.i.d.) random variables with uniform distributions over  $[-\pi, \pi)$ ,  $f_{T_{max}}$  and  $f_{R_{max}}$  are the maximum Doppler frequencies with respect to the Tx and Rx, respectively.

As introduced in [11], the impact of VTD on statistical properties can not be neglected at all taps of a wideband V2V channel. Note that VTD is a relative concept. There is no strict boundary to separate the high and low VTDs in our models. To take the impact of VTD into account, we must distinguish between the moving vehicles around the Tx (and Rx) and the stationary roadside environment. Therefore, we adopt the two-sphere model to mimic the moving vehicles and multiple confocal elliptic-cylinder models to depict the stationary roadside environment.

In summary, for the first tap, the single-bounced rays are generated from the scatterers located on either of the two spheres or the first elliptic-cylinder, while the double-bounced rays are produced from the scatterers located on both spheres. Note that only the first tap contains the LoS components, a two-sphere model with single- and double-bounced rays, and multiple confocal elliptic-cylinder models with single-bounced rays, as shown in Figs. 2 and 3. For a low VTD, vehicles can be faster (i.e., relatively higher Doppler frequency) and the value of  $K$  is large since the LoS component can bear a significant amount of power. Also, the received scattered power is mainly from waves reflected by the stationary roadside environment described by the scatterers located on the first elliptic-cylinder. The moving vehicles represented by the scatterers located on the two spheres are sparse and thus more likely to be single-bounced, rather than double-bounced. This indicates that  $\eta_{SB_{1,3}} > \max\{\eta_{SB_{1,1}}, \eta_{SB_{1,2}}\} > \eta_{DB_{1,1}}$ . For a high VTD, vehicles are relatively slow (i.e., lower Doppler frequency) and the value of  $K$  is smaller than the one in the low VTD scenario. Also, due to the dense moving vehicles, the double-bounced rays of the two-sphere model bear more energy than single-bounced rays of two-sphere and elliptic-cylinder models, i.e.,  $\eta_{DB_{1,1}} > \max\{\eta_{SB_{1,1}}, \eta_{SB_{1,2}}, \eta_{SB_{1,3}}\}$ .

For other taps, we assume that the single-bounced rays are generated only from the scatterers located on the corresponding elliptic-cylinder, while the double-bounced rays are caused by the scatterers from the combined one sphere (either of the two spheres) and the corresponding elliptic-cylinder, as illustrated in Fig. 2. Note that according to the TDL structure, the double-bounced rays in the first tap must be smaller in distance than the single-bounced rays on the next elliptic-cylinder. This is valid only if the condition  $\max\{R_T, R_R\} < \min\{a_l - a_{l-1}\}$  is fulfilled. For many current V2V channel measurement campaigns, e.g., in [11], [32], the resolution in delay is 100 ns. Then, the above condition can be modified as  $\max\{R_T, R_R\} \leq 15$  m by calculating the equality  $2(a_l - a_{l-1}) = c \cdot \tau'$  with  $c = 3 \times 10^8$  m/s and  $\tau' = 100$  ns. This indicates that the maximum acceptable width of the road is 30 m, which is sufficiently large to cover most roads in reality. In other words, the proposed wideband model with the specified TDL structure is valid for various scenarios. For a low VTD, the received scattered power is mainly from waves reflected by the stationary roadside environment described by the scatterers located on the elliptic-cylinder. This indicates that  $\eta_{SB_{1,3}} > \max\{\eta_{DB_{1,1}}, \eta_{DB_{1,2}}\}$ . For a high VTD, due to the large number of moving vehicles, the double-bounced rays from the combined one sphere and elliptic-cylinder models bear more energy than the single-bounced rays of the elliptic-cylinder model, i.e.,  $\min\{\eta_{DB_{1,1}}, \eta_{DB_{1,2}}\} > \eta_{SB_{1,3}}$ .

From Figs. 2 and 3, based on the application of the law of cosines in triangles and the following assumptions  $\min\{R_T, R_R, a - f\} \gg \max\{\delta_T, \delta_R\}$  and  $D \gg \max\{R_T, R_R\}$ , and using the approximation  $\sqrt{1+x} \approx 1+x/2$  for small  $x$ . Also, based on the law of cosines in appropriate triangles and small angle approximations (i.e.,  $\sin x \approx x$  and  $\cos x \approx 1$  for small  $x$ ), we have

$$\varepsilon_{pq} \approx \xi - \frac{\delta_R}{2\xi} \left[ \frac{\delta_T}{2} \sin \varphi_T \sin \varphi_R - Q \cos \varphi_R \cos \theta_R \right] \quad (6a)$$

$$\varepsilon_{pn_{1,1}} \approx R_T - \frac{\delta_T}{2} \left[ \sin \beta_T^{(n_{1,1})} \sin \varphi_T + \cos \beta_T^{(n_{1,1})} \cos \varphi_T \cos (\theta_T - \alpha_T^{(n_{1,1})}) \right] \quad (6b)$$

$$\varepsilon_{n_{1,1}q} \approx \xi_{n_{1,1}} - \frac{\delta_R}{2\xi_{n_{1,1}}} \left[ R_T \sin \beta_T^{(n_{1,1})} \sin \varphi_R - Q_{n_{1,1}} \cos \varphi_R \cos (\alpha_R^{(n_{1,1})} - \theta_R) \right] \quad (6c)$$

$$\varepsilon_{pn_{1,2}} \approx \xi_{n_{1,2}} - \frac{\delta_T}{2\xi_{n_{1,2}}} \left[ R_R \sin \beta_R^{(n_{1,2})} \sin \varphi_T + Q_{n_{1,2}} \cos \varphi_T \cos (\alpha_T^{(n_{1,2})} - \theta_T) \right] \quad (6d)$$

$$\varepsilon_{n_{1,2}q} \approx R_R - \frac{\delta_R}{2} \left[ \sin \beta_R^{(n_{1,2})} \sin \varphi_R + \cos \beta_R^{(n_{1,2})} \cos \varphi_R \cos (\theta_R - \alpha_R^{(n_{1,2})}) \right] \quad (6e)$$

$$\varepsilon_{n_{1,1}n_{1,2}} \approx \left\{ \left[ D - R_T \cos \alpha_T^{(n_{1,1})} - R_R \cos (\alpha_R^{(n_{1,1})} - \alpha_R^{(n_{1,2})}) \right]^2 + \left[ R_T \cos \beta_T^{(n_{1,1})} - R_R \cos \beta_R^{(n_{1,2})} \right]^2 \right\}^{1/2} \quad (6f)$$

$$\varepsilon_{pn_{1,3}} \approx \xi_T^{(n_{1,3})} - \frac{\delta_T}{2\xi_T^{(n_{1,3})}} \left[ \xi_R^{(n_{1,3})} \sin \beta_R^{(n_{1,3})} \sin \varphi_T + Q_{n_{1,3}} \cos \varphi_T \cos (\alpha_T^{(n_{1,3})} - \theta_T) \right] \quad (6g)$$

$$\varepsilon_{n_{1,3}q} \approx \xi_R^{(n_{1,3})} - \delta_R \left[ \sin \beta_R^{(n_{1,3})} \sin \varphi_R + \cos \beta_R^{(n_{1,3})} \cos \varphi_R \cos (\alpha_R^{(n_{1,3})} - \theta_R) \right] \quad (6h)$$

$$\varepsilon_{pn_{1,3}} \approx \xi_T^{(n_{1,3})} - \frac{\delta_T}{2\xi_T^{(n_{1,3})}} \left[ \xi_R^{(n_{1,3})} \sin \beta_R^{(n_{1,3})} \sin \varphi_T + Q_{n_{1,3}} \cos \varphi_T \cos (\alpha_T^{(n_{1,3})} - \theta_T) \right] \quad (6i)$$

$$\varepsilon_{n_{1,3}q} \approx \xi_R^{(n_{1,3})} - \delta_R \left[ \sin \beta_R^{(n_{1,3})} \sin \varphi_R + \cos \beta_R^{(n_{1,3})} \cos \varphi_R \cos (\alpha_R^{(n_{1,3})} - \theta_R) \right] \quad (6j)$$

where  $\xi \approx Q \approx D - \frac{\delta_T}{2} \cos \varphi_T \cos \theta_T$ ,  $\xi_{n_{1,1}} = \sqrt{Q_{n_{1,1}}^2 + R_T^2 \sin^2 \beta_T^{(n_{1,1})}}$ ,  $Q_{n_{1,1}} \approx D - R_T \cos \beta_T^{(n_{1,1})} \times \cos \alpha_T^{(n_{1,1})}$ ,  $\xi_{n_{1,2}} = \sqrt{Q_{n_{1,2}}^2 + R_R^2 \sin^2 \beta_R^{(n_{1,2})}}$ ,  $Q_{n_{1,2}} \approx D + R_R \cos \beta_R^{(n_{1,2})} \cos \alpha_R^{(n_{1,2})}$ ,  $\xi_R^{(n_{1,3})} = \frac{2a_1 - Q_{n_{1,3}}}{\cos \beta_R^{(n_{1,3})}}$ ,  $\xi_T^{(n_{1,3})} = \sqrt{Q_{n_{1,3}}^2 + (\xi_R^{(n_{1,3})})^2 \sin^2 \beta_R^{(n_{1,3})}}$ , and  $Q_{n_{1,3}} = \frac{a_1^2 + f^2 + 2a_1 f \cos \alpha_R^{(n_{1,3})}}{a_1 + f \cos \alpha_R^{(n_{1,3})}}$ .  $\alpha_T^{LoS} \approx \beta_T^{LoS} \approx \beta_R^{LoS} \approx 0$ ,  $\alpha_R^{LoS} \approx \pi$ ,  $\xi_T^{(n_{1,3})} = \frac{a_1^2 + f^2 + 2a_1 f \cos \phi_R^{(n_{1,3})}}{a_1 + f \cos \phi_R^{(n_{1,3})}}$ , and  $\xi_R^{(n_{1,3})} = \frac{b_l^2}{a_1 + f \cos \phi_R^{(n_{1,3})}}$  with  $b_l$  denoting the semi-minor axis of the  $l$ th elliptic-cylinder. Note that the azimuth/elevation angle of departure (AAoD/EAoD), (i.e.,  $\alpha_T^{(n_{l,i})}$ ,  $\beta_T^{(n_{l,i})}$ ), and azimuth/elevation

angle of arrival (AAoA/EAoA), (i.e.,  $\alpha_R^{(n_{l,i})}$ ,  $\beta_R^{(n_{l,i})}$ ), are independent for double-bounced rays, while are correlated for single-bounced rays. According to spacial solid geometrical algorithms, for the single-bounced rays resulting from the two-sphere model, we can derive the relationship between the AoDs and AoAs as  $\alpha_R^{(n_{1,1})} \approx \pi - \frac{R_T}{D} \sin \alpha_T^{(n_{1,1})}$ ,  $\beta_R^{(n_{1,1})} \approx \arccos\left(\frac{D-R_T \cos \beta_T^{(1,1)} \cos \alpha_T^{(1,1)}}{\xi_{n_{1,1}}}\right)$ , and  $\alpha_T^{(n_{1,2})} \approx \frac{R_R}{D} \sin \alpha_R^{(n_{1,2})}$ ,  $\beta_T^{(n_{1,2})} \approx \arccos\left(\frac{D+R_R \cos \beta_R^{(1,2)} \cos \alpha_R^{(1,2)}}{\xi_{n_{1,2}}}\right)$ . For the single-bounced rays resulting from elliptic-cylinder model, the angular relationship  $\alpha_T^{(n_{l,3})} = \arcsin\left(\frac{b_l^2 \sin \alpha_R^{(n_{l,3})}}{a_l^2 + f^2 + 2a_l f \cos \alpha_R^{(n_{l,3})}}\right)$  and  $\beta_T^{(n_{l,3})} = \arccos\left[\frac{a_l^2 + f^2 + 2a_l f \cos \alpha_R^{(n_{l,3})}}{(a_l + f \cos \alpha_R^{(n_{l,3})}) \xi_T^{(n_{l,3})}}\right]$  hold with  $b_l = \sqrt{a_l^2 - f^2}$  denoting the semi-minor axis of the first elliptic-cylinder.

For the proposed theoretical 3D RS-GBSM, as the number of scatterers tends to infinity, the discrete AAoD  $\alpha_T^{(n_{l,i})}$ , EAoD  $\beta_T^{(n_{l,i})}$ , AAoA  $\alpha_R^{(n_{l,i})}$ , and EAoA  $\beta_R^{(n_{l,i})}$  can be replaced by continuous random variables  $\alpha_T^{(l,i)}$ ,  $\beta_T^{(l,i)}$ ,  $\alpha_R^{(l,i)}$ , and  $\beta_R^{(l,i)}$ , respectively. To jointly consider the impact of the azimuth and elevation angles on channel statistics, we use the VMF PDF to characterize the distribution of effective scatterers, which is defined as [34]

$$f(\alpha, \beta) = \frac{k \cos \beta}{4\pi \sinh k} \times e^{k[\cos \beta_0 \cos \beta \cos(\alpha - \alpha_0) + \sin \beta_0 \sin \beta]} \quad (7)$$

where  $\alpha, \beta \in [-\pi, \pi)$ ,  $\alpha_0 \in [-\pi, \pi)$ , and  $\beta_0 \in [-\pi, \pi)$  account for the mean values of the azimuth angle  $\alpha$  and elevation angle  $\beta$ , respectively, and  $k$  ( $k \geq 0$ ) is a real-valued parameter that controls the concentration of the distribution identified by the mean direction  $\alpha_0$  and  $\beta_0$ .

In this paper, for the angular descriptions, i.e., the AAoD  $\alpha_T^{(1,1)}$  and EAoD  $\beta_T^{(1,1)}$  for the Tx sphere, the AAoA  $\alpha_R^{(1,2)}$  and EAoA  $\beta_R^{(1,2)}$  for the Rx sphere, and the AAoA  $\alpha_R^{(l,3)}$  and EAoA  $\beta_R^{(l,3)}$  for multiple elliptic cylinders, the parameters ( $\alpha_0$ ,  $\beta_0$ , and  $k$ ) of the VMF PDF in (7) can be replaced by  $(\alpha_{T0}^{(l,1)}$ ,  $\beta_{T0}^{(l,1)}$ , and  $k^{(l,1)}$ ),  $(\alpha_{R0}^{(l,2)}$ ,  $\beta_{R0}^{(l,2)}$ , and  $k^{(l,2)}$ ), and  $(\alpha_{R0}^{(l,3)}$ ,  $\beta_{R0}^{(l,3)}$ , and  $k^{(l,3)}$ ), respectively.

### C. Non-Stationary Time-Varying Parameters

Based on the proposed 3D wideband V2V channel model, it is feasible to develop the corresponding non-WSS model by imposing the time-varying parameters.

1) *Total Number of Taps*: In [11], V2V channel measurements have proved that the total number of taps has the non-stationary tap persistence feature. A genetic appearance (birth) and disappearance (death) process for modeling the multipath components (MPCs) was proposed in [36]. Since in a time-variant (i.e., non-stationary) scenario, all MPCs only exist over a certain time period. With ongoing time, MPCs appear and remain for a certain time span and then finally disappear. A suitable description for such a generation-recombination behavior is given by discrete Markov processes. In V2V channel,

the time variation of a wireless V2V channel is mainly caused by movements of the Tx, Rx and moving scatterers. Therefore, the movement of scenarios is introduced and applied mathematically. The process of MPCs generation and recombination, i.e., time dependent channel fluctuations, is caused by the movement of the Tx ( $\Delta_{T,k}$ ) as well as the movement of the Rx ( $\Delta_{R,k}$ ) in the time span between  $t_{k-1}$  and  $t_k$ , i.e.,

$$\Delta_{P,k} = \Delta_{T,k} + \Delta_{R,k} \quad (8)$$

with

$$\Delta_{T,k} = \int_{t_{k-1}}^{t_k} P_c \cdot \bar{v}_T dt \quad (9)$$

and

$$\Delta_{R,k} = \int_{t_{k-1}}^{t_k} (|\bar{x}_R(t)|) dt \quad (10)$$

where  $P_c$  is a percentage of MPCs contains moving scatterers with a mean velocity  $\bar{v}_T$  and  $\bar{x}_R(t)$  is the motion difference of the Rx. Because of the short time slot, a constant motion in each time interval  $|t_k - t_{k-1}|$  is assumed. This simplifies (9) and (10) to

$$\Delta_{T,k} = (t_k - t_{k-1}) P_c \bar{v}_T \quad (11)$$

$$\Delta_{R,k} = |\bar{x}_R(t_k) - \bar{x}_R(t_{k-1})|. \quad (12)$$

Therefore,  $\Delta_{P,k}$  gives a measure for the correlation of channel impulse responses (CIRs) at different time snapshots. A Markov birth-death description [36] results in a time-varying number  $L(t)$  of MPCs for CIR realizations. At any time instant  $t_k$ , one can distinguish between newly generated MPCs and MPCs that were already existing in the previous CIR at time instant  $t_{k-1}$ . The latter are known as inherited paths. The Markov process is described by a generation rate of MPCs ( $\lambda_G$ ) and a recombination rate of new paths ( $\lambda_R$ ). The expectation of the total number, also defined as the initial number, of MPCs in a CIR realization is given by

$$\mathbf{E}\{L(t)\} = L(t_0) = \frac{\lambda_G}{\lambda_R}. \quad (13)$$

where  $\mathbf{E}[\cdot]$  designates the statistical expectation operator.

Observing a time series of CIRs, each MPC remains from one CIR at  $t_{k-1}$  to a following one at  $t_k$  with the probability:

$$P_{\text{remain}}(\Delta_{P,k}) = e^{-\lambda_R \cdot \Delta_{P,k}}. \quad (14)$$

Hence, a number of new MPCs is generated by the Markov process with expectation

$$\mathbf{E}\{L_{\text{new}k}\} = \frac{\lambda_G}{\lambda_R} (1 - e^{-\lambda_R \cdot \Delta_{P,k}}). \quad (15)$$

The correlation between two evolving MPCs is quantified by the scenario movement  $\Delta_{P,k}$ . Mathematically, higher values of  $\Delta_{P,k}$  result in a reduced correlation between the properties of an ancestor MPC at  $t_{k-1}$  and its successor at  $t_k$ . Therefore, the total number of taps  $L(t)$  in (1) is time-variant demonstrating the non-stationarity of the V2V channels.

2) *Time-Varying AoDs and AoAs*: To derive time-varying AoDs and AoAs, we have to assume a V2V communication

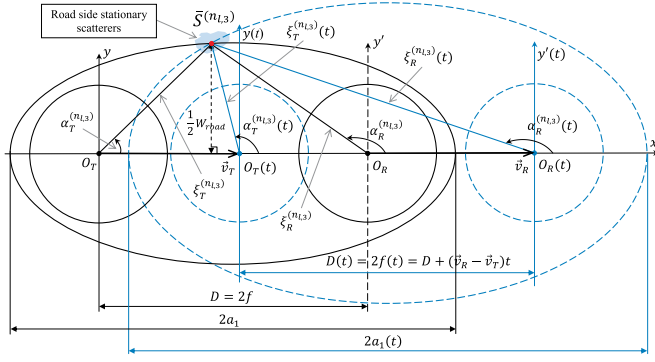


Fig. 4. The non-stationary geometry of the single-bounced rays in the  $l$ th tap elliptic-cylinder model.

scenario. Fig. 4 presents the projection of a V2V communication with the Tx and Rx driving in the same direction along a straight road. In addition, the Rx always drives equally or faster than the Tx so that a car crash will never happen with time going. Please note that Fig. 4 only shows the time-varying AAoDs and AAoAs of the elliptic-cylinder model as the figure is the horizontal projection of the 3D model. Due to the over-complex issues, the corresponding 3D figure with MIMO antennas are omitted here for brevity. Based on the theory of relative motion and geometrical relationship in the model, the time-varying AoDs and AoAs can be derived in terms of the scenario in Fig. 4 as follows.

- In the case of the LoS components, time-varying AAoD ( $\alpha_T^{LoS}(t)$ ), EAoD ( $\beta_T^{LoS}(t)$ ), AAoA ( $\alpha_R^{LoS}(t)$ ), and EAoA ( $\beta_R^{LoS}(t)$ ) can be expressed as  $\alpha_T^{LoS}(t) \approx \beta_T^{LoS}(t) \approx \beta_R^{LoS}(t) = 0$ , and  $\alpha_R^{LoS}(t) = \pi$ .
- In the case of the single-bounced components  $SB_{1,i}$  ( $i = 1, 2$ ) resulting from the Tx sphere and Rx sphere, respectively, time-varying AAoD ( $\alpha_T^{(n_{1,i})}(t)$ ), EAoD ( $\beta_T^{(n_{1,i})}(t)$ ), AAoA ( $\alpha_R^{(n_{1,i})}(t)$ ), and EAoA ( $\beta_R^{(n_{1,i})}(t)$ ) can be expressed as  $\alpha_T^{(n_{1,i})}(t) \approx \alpha_T^{(n_{1,i})}$ ,  $\beta_T^{(n_{1,i})}(t) \approx \beta_T^{(n_{1,i})}$ ,  $\alpha_R^{(n_{1,i})}(t) \approx \alpha_R^{(n_{1,i})}$ , and  $\beta_R^{(n_{1,i})}(t) \approx \beta_R^{(n_{1,i})}$ .
- In the case of the single-bounced components  $SB_{l,3}$  for the  $l$ th tap resulting from the elliptic-cylinder, time-varying AAoA ( $\alpha_R^{(n_{l,3})}(t)$ ) and EAoA ( $\beta_R^{(n_{l,3})}(t)$ ) can be expressed as

$$\alpha_R^{(n_{l,3})}(t) = \pi - \arccos \frac{v_R t - \xi_R^{(n_{l,3})} \cos \alpha_R^{(n_{l,3})}}{\sqrt{\xi_R^{(n_{l,3})^2 + (v_R t)^2 - 2\xi_R^{(n_{l,3})} v_R t \cos \alpha_R^{(n_{l,3})}}} \quad (16a)$$

$$\beta_R^{(n_{l,3})}(t) = \arctan \frac{\xi_R^{(n_{l,3})} \tan \beta_R^{(n_{l,3})}}{\sqrt{\xi_R^{(n_{l,3})^2 + (v_R t)^2 - 2\xi_R^{(n_{l,3})} v_R t \cos \alpha_R^{(n_{l,3})}}} \quad (16b)$$

Note that the time-varying AAoD ( $\alpha_T^{(n_{l,3})}(t)$ ) and EAoD ( $\beta_T^{(n_{l,3})}(t)$ ), are correlated with time-varying AAoA ( $\alpha_R^{(n_{l,3})}(t)$ ) and EAoA ( $\beta_R^{(n_{l,3})}(t)$ ) for single-bounced rays resulting from the elliptic-cylinder model. Hence, the

relationship between the AoD and AoA for multiple confocal elliptic-cylinder models can be given by

$$\alpha_T^{(n_{l,3})}(t) = \arcsin \frac{b(t)^2 \sin \alpha_R^{(n_{l,3})}(t)}{a(t)^2 + f(t)^2 + 2a(t)f(t) \cos \alpha_R^{(n_{l,3})}(t)} \quad (17a)$$

$$\beta_T^{(n_{l,3})}(t) = \arccos \frac{a(t)^2 + f(t)^2 + 2a(t)f(t) \cos \alpha_R^{(n_{l,3})}(t)}{(a(t) + f(t) \cos \alpha_R^{(n_{l,3})}(t)) \xi_T^{(n_{l,3})}(t)} \quad (17b)$$

- In terms of the double-bounced component  $DB_{1,1}$  for the first tap resulting from the Tx and Rx spheres, time-varying AAoD ( $\alpha_T^{(n_{1,1})}(t)$ ), EAoD ( $\beta_T^{(n_{1,1})}(t)$ ), AAoA ( $\alpha_R^{(n_{1,2})}(t)$ ), and EAoA ( $\beta_R^{(n_{1,2})}(t)$ ) can be expressed as  $\alpha_T^{(n_{1,1})}(t) \approx \alpha_T^{(n_{1,1})}$ ,  $\beta_T^{(n_{1,1})}(t) \approx \beta_T^{(n_{1,1})}$ ,  $\alpha_R^{(n_{1,2})}(t) \approx \beta_R^{(n_{1,2})}$ , and  $\beta_R^{(n_{1,2})}(t) \approx \beta_R^{(n_{1,2})}$ .
- In terms of the double-bounced component  $DB_{l,1}$  for other taps resulting from the Tx sphere and elliptic-cylinder, time-varying AAoD ( $\alpha_T^{(n_{l,1})}(t)$ ), EAoD ( $\beta_T^{(n_{l,1})}(t)$ ), AAoA ( $\alpha_R^{(n_{l,3})}(t)$ ), and EAoA ( $\beta_R^{(n_{l,3})}(t)$ ) can be expressed as

$$\alpha_T^{(n_{l,1})}(t) = \alpha_T^{(n_{l,1})}(t) = \alpha_T^{(n_{l,1})} \quad (18a)$$

$$\beta_T^{(n_{l,1})}(t) = \beta_T^{(n_{l,1})}(t) = \beta_T^{(n_{l,1})} \quad (18b)$$

$$\alpha_R^{(n_{l,3})}(t) = \pi - \arccos \frac{v_R t - \xi_R^{(n_{l,3})} \cos \alpha_R^{(n_{l,3})}}{\sqrt{\xi_R^{(n_{l,3})^2 + (v_R t)^2 - 2\xi_R^{(n_{l,3})} v_R t \cos \alpha_R^{(n_{l,3})}}} \quad (18c)$$

$$\beta_R^{(n_{l,3})}(t) = \arctan \frac{\xi_R^{(n_{l,3})} \tan \beta_R^{(n_{l,3})}}{\sqrt{\xi_R^{(n_{l,3})^2 + (v_R t)^2 - 2\xi_R^{(n_{l,3})} v_R t \cos \alpha_R^{(n_{l,3})}}} \quad (18d)$$

- In terms of the double-bounced component  $DB_{l,2}$  for other taps resulting from the elliptic-cylinder and Rx sphere, time-varying AAoD ( $\alpha_T^{(n_{l,2})}(t)$ ), EAoD ( $\beta_T^{(n_{l,2})}(t)$ ), AAoA ( $\alpha_R^{(n_{l,2})}(t)$ ), and EAoA ( $\beta_R^{(n_{l,2})}(t)$ ) can be expressed as

$$\alpha_T^{(n_{l,2})}(t) = \arcsin \frac{b(t)^2 \sin \alpha_R^{(n_{l,2})}(t)}{a(t)^2 + f(t)^2 + 2a(t)f(t) \cos \alpha_R^{(n_{l,2})}(t)} \quad (19a)$$

$$\beta_T^{(n_{l,2})}(t) = \arccos \frac{a(t)^2 + f(t)^2 + 2a(t)f(t) \cos \alpha_R^{(n_{l,2})}(t)}{(a(t) + f(t) \cos \alpha_R^{(n_{l,2})}(t)) \xi_T^{(n_{l,2})}(t)} \quad (19b)$$

$$\alpha_R^{(n_{l,2})}(t) = \alpha_R^{(n_{l,2})}(t) = \alpha_R^{(n_{l,2})} \quad (19c)$$

$$\beta_R^{(n_{l,2})}(t) = \beta_R^{(n_{l,2})}(t) = \beta_R^{(n_{l,2})} \quad (19d)$$

Again, the two-sphere model describes the moving scatterers around the Tx and Rx, and the elliptic-cylinder model depicts the static roadside scatterers. Therefore, the AoDs and AoAs of LoS component and the two-sphere model including both single- and double-bounced rays are actually time-invariant due to the feature of relative rest. The reason behind is that we assume moving vehicles/scatterers around the Tx and Rx having the same velocity (i.e., both in speed and direction) of the Tx and Rx, respectively. Therefore, the original fixed parameters can be replaced by these time-varying parameters so that the proposed model is able to capture the channel non-stationarity.

### III. LOCAL STATISTICAL PROPERTIES OF THE PROPOSED 3D WIDEBAND NON-WSS MIMO V2V CHANNEL MODEL

#### A. Local ST CF

The local correlation properties of two arbitrary CIRs  $h_{pq}(t, \tau)$  and  $h_{p'q'}(t, \tau')$  of a MIMO V2V channel are completely determined by the correlation properties of  $h_{l,pq}(t)$  and  $h_{l,p'q'}(t)$  in each tap, so that no correlations exist between the underlying processes in different taps. Therefore, we can restrict our investigations to the following local ST CF:

$$\rho_{h_{l,pq}h_{l,p'q'}}(t, \tau) = \mathbf{E} \left[ h_{l,pq}(t) h_{l,p'q'}^*(t - \tau) \right] \quad (20)$$

where  $(\cdot)^*$  denotes the complex conjugate operation. Since the LoS, single-, and double-bounced components are independent to each other, based on (2) we have the following local ST CF for the first tap

$$\begin{aligned} \rho_{h_{1,pq}h_{1,p'q'}}(t, \tau) &= \rho_{h_{1,pq}^{LoS}h_{1,p'q'}^{LoS}}(t, \tau) \\ &+ \sum_{i=1}^I \rho_{h_{1,pq}^{SB_i}h_{1,p'q'}^{SB_i}}(t, \tau) + \rho_{h_{1,pq}^{DB}h_{1,p'q'}^{DB}}(t, \tau). \end{aligned} \quad (21)$$

Whereas for other taps, according to (4) we have the ST CF as

$$\begin{aligned} \rho_{h_{l,pq}h_{l,p'q'}}(t, \tau) &= \rho_{h_{l,pq}^{SB_3}h_{l,p'q'}^{SB_3}}(t, \tau) \\ &+ \rho_{h_{l,pq}^{DB_1}h_{l,p'q'}^{DB_1}}(t, \tau) + \rho_{h_{l,pq}^{DB_2}h_{l,p'q'}^{DB_2}}(t, \tau). \end{aligned} \quad (22)$$

Applying the corresponding VMF distribution, trigonometric transformations, and following the similar reasoning in [10], we can obtain the local ST CF of the LoS, single-, and double-bounced components as follows.

(a) In the case of the LoS component,

$$\rho_{h_{1,pq}^{LoS}h_{1,p'q'}^{LoS}}(t, \tau) = Ke^{\frac{j2\pi}{\lambda}A^{LoS}} e^{j2\pi\tau(f_{Tmax} \cos \gamma_T - f_{Rmax} \cos \gamma_R)} \quad (23)$$

where  $A^{LoS} = 2D \cos \varphi_R \cos \theta_R$ .

(b) In terms of the single-bounced components  $SB_{1,i}$  ( $i = 1, 2$ ) for the first tap resulting from the Tx sphere and Rx

sphere, respectively,

$$\begin{aligned} \rho_{h_{1,pq}^{SB_{1,i}}h_{1,p'q'}^{SB_{1,i}}}(t, \tau) &= \eta_{SB_{1,i}} \int_{-\pi}^{\pi} \int_{-\pi}^{\pi} \left[ e^{\frac{j2\pi}{\lambda}A^{(1,i)}} \right. \\ &\times e^{j2\pi\tau(f_{Tmax}B^{(1,i)} + f_{Rmax}C^{(1,i)})} \\ &\times f(\alpha_{T/R}^{(1,i)}, \beta_{T/R}^{(1,i)}) \left. \right] d(\alpha_{T/R}^{(1,i)}, \beta_{T/R}^{(1,i)}) \end{aligned} \quad (24)$$

with  $A^{(1,1)} = \delta_T [\sin \beta_T^{(1,1)} \sin \varphi_T + \cos \beta_T^{(1,1)} \cos \varphi_T \times \cos(\theta_T - \alpha_T^{(1,1)})] + \frac{\delta_R}{\xi_{n_{1,1}}} [R_T \sin \beta_T^{(1,1)} \sin \varphi_R - Q_{n_{1,1}} \times \cos \varphi_R \cos(\theta_R - \alpha_R^{(1,1)})]$ ,  $B^{(1,i)} = \cos(\alpha_T^{(1,i)} - \gamma_T) \cos(\beta_T^{(1,i)})$ ,  $C^{(1,i)} = \cos(\alpha_R^{(1,i)} - \gamma_R) \cos(\beta_R^{(1,i)})$ ,  $A^{(1,2)} = \delta_R [\sin \beta_R^{(1,2)} \sin \varphi_R + \cos \beta_R^{(1,2)} \cos \varphi_R \cos(\theta_R - \alpha_R^{(1,2)})] + \frac{\delta_T}{\xi_{n_{1,2}}} [R_R \sin \beta_R^{(1,2)} \sin \varphi_T + Q_{n_{1,2}} \cos \varphi_T \cos(\theta_T - \alpha_T^{(1,2)})]$ , where the expressions of  $\alpha_R^{(1,i)}$ ,  $\beta_R^{(1,i)}$ ,  $Q_{n_{1,i}}$ ,  $\xi_{n_{1,i}}$ , and  $\xi_{T(R)}^{n_{1,3}}$  are given in Section II. Note that the subscripts  $T$  and  $R$  are applied to  $i = 1$  and  $i = 2$ , respectively.

(c) In the case of the single-bounced component  $SB_{l,3}$  for the  $l$ th tap resulting from the elliptic-cylinder,

$$\begin{aligned} \rho_{h_{l,pq}^{SB_{l,3}}h_{l,p'q'}^{SB_{l,3}}}(t, \tau) &= \eta_{SB_{l,3}} \int_{-\pi}^{\pi} \int_{-\pi}^{\pi} \left[ e^{-\frac{j2\pi}{\lambda}A^{(l,3)}} \right. \\ &\times e^{j2\pi\tau(f_{Tmax}B^{(l,3)} + f_{Rmax}C^{(l,3)})} \\ &\times f(\alpha_R^{(l,3)}, \beta_R^{(l,3)}) \left. \right] d(\alpha_R^{(l,3)}, \beta_R^{(l,3)}) \end{aligned} \quad (25)$$

with  $A^{(l,3)} = \frac{\delta_T}{\xi_{T(R)}^{(n_{l,3})}} [\xi_R^{(n_{l,3})} \sin \beta_R^{(l,3)} \sin \varphi_T + Q_{n_{l,3}} \cos \varphi_T \times \cos(\theta_T - \alpha_T^{(l,3)})] + \delta_R [\sin \beta_R^{(l,3)} \sin \varphi_R + \cos \beta_R^{(l,3)} \cos \varphi_R \times \cos(\theta_R - \alpha_R^{(l,3)})]$ ,  $B^{(l,3)} = \cos(\alpha_T^{(l,3)} - \gamma_T) \cos(\beta_T^{(l,3)})$ ,  $C^{(l,3)} = \cos(\alpha_R^{(l,3)} - \gamma_R) \cos(\beta_R^{(l,3)})$ , where the expressions of  $\alpha_T^{(l,3)}$ ,  $\beta_T^{(l,3)}$ ,  $Q_{n_{l,3}}$ , and  $\xi_{T(R)}^{(n_{l,3})}$  are given in Section II-A.

(d) In terms of the double-bounced component  $DB_{1,1}$  for the first tap resulting from the Tx and Rx spheres,

$$\begin{aligned} \rho_{h_{1,pq}^{DB}h_{1,p'q'}^{DB}}(t, \tau) &= \eta_{DB_{1,1}} \int_{-\pi}^{\pi} \int_{-\pi}^{\pi} \int_{-\pi}^{\pi} \int_{-\pi}^{\pi} \left[ e^{\frac{j2\pi}{\lambda}A^{DB}} \right. \\ &\times e^{j2\pi\tau(f_{Tmax}B^{DB} + f_{Rmax}C^{DB})} \\ &\times f(\alpha_T^{(1,1)}, \beta_T^{(1,1)}) \cdot f(\alpha_R^{(1,2)}, \beta_R^{(1,2)}) \left. \right] \\ &d(\alpha_T^{(1,1)}, \beta_T^{(1,1)}) d(\alpha_R^{(1,2)}, \beta_R^{(1,2)}) \end{aligned} \quad (26)$$

where  $A^{DB} = \delta_T [\sin \beta_T^{(1,1)} \sin \varphi_T + \cos \beta_T^{(1,1)} \cos \varphi_T \times \cos(\theta_T - \alpha_T^{(1,1)})] + \delta_R [\sin \beta_R^{(1,2)} \sin \varphi_R + \cos \beta_R^{(1,2)} \times \cos \varphi_R \cos(\theta_R - \alpha_R^{(1,2)})]$ ,  $B^{DB} = \cos(\alpha_T^{(1,1)} - \gamma_T) \cos \beta_T^{(1,1)}$ , and  $C^{DB} = \cos(\alpha_R^{(1,2)} - \gamma_R) \cos \beta_R^{(1,2)}$ .

- (e) In terms of the double-bounced component  $DB_{l,1}$  for other taps resulting from the Tx sphere and elliptic-cylinder,

$$\begin{aligned} \rho_{h_{l,pq}^{DB_1} h_{l,p'q'}^{DB_1}}(t, \tau) &= \eta_{DB_{l,1}} \int_{-\pi}^{\pi} \int_{-\pi}^{\pi} \int_{-\pi}^{\pi} \int_{-\pi}^{\pi} \left[ e^{\frac{j2\pi}{\lambda} A^{DB_{l,1}}} \right. \\ &\quad \times e^{j2\pi\tau(f_{T_{\max}} B^{DB_{l,1}} + f_{R_{\max}} C^{DB_{l,1}})} \\ &\quad \times f\left(\alpha_T^{(1,1)}, \beta_T^{(1,1)}\right) \cdot f\left(\alpha_R^{(l,3)}, \beta_R^{(l,3)}\right) \\ &\quad \left. d\left(\alpha_T^{(1,1)}, \beta_T^{(1,1)}\right) d\left(\alpha_R^{(l,3)}, \beta_R^{(l,3)}\right) \right] \end{aligned} \quad (27)$$

where  $A^{DB_{l,1}} = \delta_T [\sin \beta_T^{(1,1)} \sin \varphi_T + \cos \beta_T^{(1,1)} \cos \varphi_T \times \cos(\theta_T - \alpha_T^{(1,1)})] + \delta_R [\sin \beta_R^{(l,3)} \sin \varphi_R + \cos \beta_R^{(l,3)} \cos \varphi_R \times \cos(\theta_R - \alpha_R^{(l,3)})]$ ,  $B^{DB_{l,1}} = \cos(\alpha_T^{(1,1)} - \gamma_T) \cos \beta_T^{(1,1)}$ , and  $C^{DB_{l,1}} = \cos(\alpha_R^{(l,3)} - \gamma_R) \cos \beta_R^{(l,3)}$ .

- (f) In terms of the double-bounced component  $DB_{l,2}$  for other taps resulting from the elliptic-cylinder and Rx sphere,

$$\begin{aligned} \rho_{h_{l,pq}^{DB_2} h_{l,p'q'}^{DB_2}}(t, \tau) &= \eta_{DB_{l,2}} \int_{-\pi}^{\pi} \int_{-\pi}^{\pi} \int_{-\pi}^{\pi} \int_{-\pi}^{\pi} \left[ e^{\frac{j2\pi}{\lambda} A^{DB_{l,2}}} \right. \\ &\quad \times e^{j2\pi\tau(f_{T_{\max}} B^{DB_{l,2}} + f_{R_{\max}} C^{DB_{l,2}})} \\ &\quad \times f\left(\alpha_T^{(l,3)}, \beta_T^{(l,3)}\right) \cdot f\left(\alpha_R^{(1,2)}, \beta_R^{(1,2)}\right) \\ &\quad \left. d\left(\alpha_T^{(l,3)}, \beta_T^{(l,3)}\right) d\left(\alpha_R^{(1,2)}, \beta_R^{(1,2)}\right) \right] \end{aligned} \quad (28)$$

where  $A^{DB_{l,2}} = \delta_T [\sin \beta_T^{(l,3)} \sin \varphi_T + \cos \beta_T^{(l,3)} \cos \varphi_T \times \cos(\theta_T - \alpha_T^{(l,3)})] + \delta_R [\sin \beta_R^{(1,2)} \sin \varphi_R + \cos \beta_R^{(1,2)} \cos \varphi_R \times \cos(\theta_R - \alpha_R^{(1,2)})]$ ,  $B^{DB_{l,2}} = \cos(\alpha_T^{(l,3)} - \gamma_T) \cos \beta_T^{(l,3)}$ , and  $C^{DB_{l,2}} = \cos(\alpha_R^{(1,2)} - \gamma_R) \times \cos \beta_R^{(1,2)}$ .

Finally, the local ST CF of the CIRs  $h_{pq}(t, \tau')$  and  $h_{p'q'}(t, \tau')$  can be expressed as:

$$\rho_{h_{pq} h_{p'q'}}(t, \tau) = \sum_{l=1}^{L(t)} c_l^2 \rho_{h_{l,pq} h_{l,p'q'}}(t, \tau). \quad (29)$$

### B. Local FCF and PDP

The local FCF  $\rho_{H_{pq} H_{p'q'}}(t, \Delta f')$  of the proposed wideband V2V channel model is defined as

$$\rho_{H_{pq} H_{p'q'}}(t, \Delta f') = \mathbf{E} \left[ H_{pq}(t, f') H_{pq}^*(t, f' - \Delta f') \right] \quad (30)$$

where,  $H_{pq}(t, f')$  denotes the time-variant transfer function, which is the Fourier transform of the CIR  $h_{pq}(t, \tau')$  and can be expressed as  $H_{pq}(t, f') = \sum_{l=1}^{L(t)} c_l h_{l,pq}(t) e^{-j2\pi f' \tau'}$ . Therefore, the local FCF can be derived as

$$\rho_{H_{pq} H_{p'q'}}(t, \Delta f') = \sum_{l=1}^{L(t)} c_l^2(t) e^{-j2\pi f' \tau'_l}. \quad (31)$$

Applying the inverse Fourier transform to the local FCF  $\rho_{H_{pq} H_{p'q'}}(\Delta f')$  in (31), we can obtain the corresponding local

PDP as

$$S_{H_{pq} H_{p'q'}}(t, \tau') = \sum_{l=1}^{L(t)} c_l^2(t) \delta(\tau' - \tau'_l). \quad (32)$$

It is obvious that the local FCF and the local PDP are completely determined by the number of propagation paths  $L(t)$  (i.e., taps), the path gains  $c_l$ , and the propagation delays  $\tau'_l$ . Appropriate values for these parameters can be found in many measurement campaigns for wideband V2V channels, e.g., those in [11], [24], [32]. This allows us to fit the local FCF  $\rho_{H_{pq} H_{p'q'}}(t, \Delta f')$  and the corresponding local PDP  $S_{H_{pq} H_{p'q'}}(t, \tau')$  of the proposed model to any specified or measured FCF and PDP characterised by the sets  $\{c_l\}_{l=1}^{L(t)}$  and  $\{\tau'_l\}_{l=1}^{L(t)}$ .

### IV. 3D WIDEBAND NON-WSS SoS SIMULATION MODEL FOR MIMO V2V CHANNELS

Based on the proposed 3D theoretical RS-GBSM described in Section II, the corresponding SoS simulation model can be further developed by using finite numbers of scatterers or sinusoids  $N_{l,1}$ ,  $N_{l,2}$ , and  $N_{l,3}$ . According to (1), the SoS simulation model for the link  $T_p \rightarrow T_q$  can be expressed as

$$\hat{h}_{pq}(t, \tau') = \sum_{l=1}^{L(t)} c_l \hat{h}_{l,pq}(t) \delta(\tau' - \tau'_l) \quad (33)$$

where for the first tap and other taps can be expressed respectively

$$\hat{h}_{1,pq}(t) = \hat{h}_{1,pq}^{LoS}(t) + \sum_{i=1}^I \hat{h}_{1,pq}^{SB_i}(t) + \hat{h}_{1,pq}^{DB}(t) \quad (34)$$

$$\hat{h}_{l,pq}(t) = \hat{h}_{l,pq}^{SB_3}(t) + \hat{h}_{l,pq}^{DB_1}(t) + \hat{h}_{l,pq}^{DB_2}(t). \quad (35)$$

Actually, the unknown simulation model parameters to be determined are only the discrete AoDs and AoAs, while the remaining parameters are identical to those of the theoretical model. Therefore, a proper parameter computation method has to be applied to obtain these discrete AoDs and AoAs.

#### A. MEV for Parameterization of the Proposed SoS Simulation Model

VMF distribution is adopted in order to jointly consider the impact of the azimuth and elevation angles on channel statistics. Furthermore, the cumulative distribution function (CDF) of  $\alpha$  and  $\beta$ , i.e., the double integral of the 3D VMF PDF, denotes the value of volume. The idea of MEV is designed to select the set of  $\{\alpha^{(n_{1,i})}, \beta^{(n_{1,i})}\}_{n_{1,i}=1}^{N_{1,i}}$  in such a manner that the volume of the VMF PDF  $f(\alpha, \beta)$  in different ranges of  $\{\alpha^{(n_{1,i-1})}, \beta^{(n_{1,i-1})}\} \leq \{\alpha, \beta\} < \{\alpha^{(n_{1,i})}, \beta^{(n_{1,i})}\}$  are equal to each other with the initial condition, i.e.,

$$\int_{-\pi}^{\alpha^{(1,1)}} \int_{-\pi}^{\beta^{(1,1)}} f(\alpha, \beta) d\alpha d\beta = \frac{1 - 1/4}{N_{1,i}}. \quad (36)$$

The detailed procedure of MEV can be found in [10]. In this paper, the MEV is also applied to obtain the proposed 3D wideband non-WSS V2V simulation model.

TABLE II  
KEY PARAMETERS OF DIFFERENT VTD SCENARIOS

	$K$	$k^{(l,1)}$	$k^{(l,2)}$	$k^{(l,3)}$	$\eta_{SB_{1,1}}$	$\eta_{SB_{1,2}}$	$\eta_{SB_{1,3}}$	$\eta_{DB_{1,1}}$	$\eta_{SB_{1,3}}$	$\eta_{DB_{1,1}}$	$\eta_{DB_{1,2}}$
Low VTD	3.786	9.6	3.6	11.5	0.335	0.203	0.411	0.051	0.758	0.121	0.121
High VTD	1.351	0.6	1.3	11.5	0.126	0.126	0.063	0.685	0.088	0.466	0.456

### B. Local Statistical Properties of the Proposed SoS Simulation Model

Based on our 3D MIMO V2V theoretical RS-GBSM and MEV, it is achievable to derive the corresponding statistical properties for the SoS simulation model by applying the discrete angular parameters to (2), and (4). As the detailed derivations have been explained in Section III for the theoretical model, those of the corresponding simulation model with similar derivations are neglected due to the page limitation.

## V. NUMERICAL RESULTS AND ANALYSIS

### A. Model Validation Using Local Stationary Time

Stationary interval (SI) is an important concept for non-WSS channel models. It is the maximum time length within which the correlation of channel coefficients exceeds a pre-defined threshold. In [24], it is defined as stationarity region length (SRL). Note that our non-WSS model is only support the scenarios 2 and 3 in [24] as the proposed model only can capture the non-stationarity when the Tx and Rx are driving in same direction. Moreover, it is worth mentioning that the measured scenarios 2 and 3 in [24], i.e., highway and urban, are corresponding to the low VTD and high VTD in our case. To validate the proposed non-WSS models in terms of the derived local statistical properties, the following parameters can be used to match the measurements in [24]. Unless otherwise specified, basic parameters in this section are obtained using  $f_c = 5.2$  GHz,  $f_{T_{max}} = f_{R_{max}} = 433$  Hz for low VTD,  $f_{T_{max}} = f_{R_{max}} = 144$  Hz for high VTD,  $D = 300$  m,  $a_1 = 160$  m,  $a_2 = 180$  m,  $R_T = R_R = 10$  m,  $\gamma_T = \gamma_R = 0^\circ$ ,  $\varphi_T = \varphi_R = 45^\circ$ ,  $\theta_T = \theta_R = 45^\circ$ ,  $\alpha_{T0}^{(1)} = 21.7^\circ$ ,  $\beta_{T0}^{(1)} = 6.7^\circ$ ,  $\alpha_{R0}^{(2)} = 147.8^\circ$ ,  $\beta_{R0}^{(2)} = 17.2^\circ$ ,  $\alpha_{R0}^{(3)} = 171.6^\circ$ , and  $\beta_{R0}^{(3)} = 31.6^\circ$ . Considering the constraints of the Ricean factor and power-related parameters to fit the measurements in [24], we have  $k^{(1,1)} = 9.6$ ,  $k^{(1,2)} = 3.6$ ,  $k^{(1,3)} = 11.5$ ,  $K = 3.786$ ,  $\eta_{SB_{1,1}} = 0.335$ ,  $\eta_{SB_{1,2}} = 0.203$ ,  $\eta_{SB_{1,3}} = 0.411$ , and  $\eta_{DB_{1,1}} = 0.051$  for tap one low VTD. For tap one high VTD, we have  $k^{(1,1)} = 0.6$ ,  $k^{(1,2)} = 1.3$ ,  $k^{(1,3)} = 11.5$ ,  $K = 1.351$ ,  $\eta_{SB_{1,1}} = 0.126$ ,  $\eta_{SB_{1,2}} = 0.126$ ,  $\eta_{SB_{1,3}} = 0.063$ , and  $\eta_{DB_{1,1}} = 0.685$ . For tap two low VTD, we have  $k^{(2,1)} = 9.6$ ,  $k^{(2,2)} = 3.6$ ,  $k^{(2,3)} = 11.5$ ,  $\eta_{SB_{2,3}} = 0.758$ , and  $\eta_{DB_{2,1}} = \eta_{DB_{2,2}} = 0.121$ . For tap two high VTD, we have  $k^{(2,1)} = 0.6$ ,  $k^{(2,2)} = 1.3$ ,  $k^{(2,3)} = 11.5$ ,  $\eta_{SB_{2,3}} = 0.088$ , and  $\eta_{DB_{2,1}} = \eta_{DB_{2,2}} = 0.456$ . Table II summarizes key parameters adopted by low and high VTD scenarios. The environment-related parameters  $k^{(l,1)}$ ,  $k^{(l,2)}$ , and  $k^{(l,3)}$  are related to the distribution of scatterers (normally, the smaller values of  $k^{(l,1)}$  and  $k^{(l,2)}$  the more dense moving vehicles/scatterers, i.e., the higher VTD). In both high and low VTDs,  $k^{(l,3)}$  is large as the scatterers reflected from static roadsides are normally concentrated. Also, Ricean factor  $K$  is small in higher VTD, as

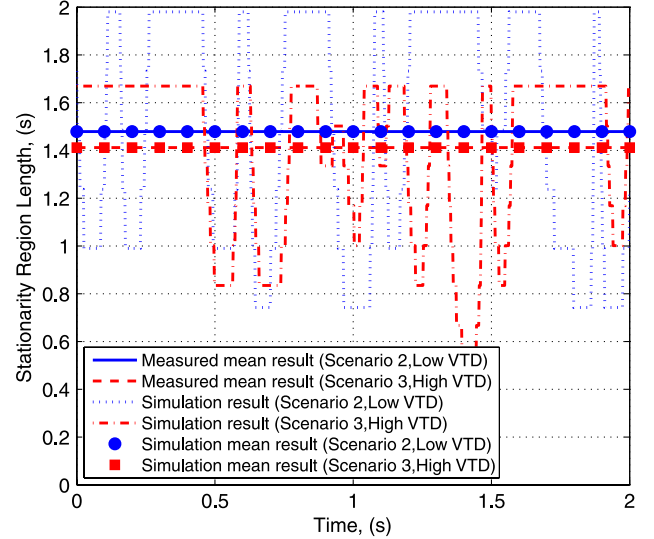


Fig. 5. The SRL of measured results and the simulation results (corresponding to scenarios 2 and 3 in [24]).

the LoS component does not have dominant power. The reason is that dense vehicles (i.e., more vehicles/obstacles between the Tx and Rx) on the road result in less likelihood of strong LoS components.

For the SoS simulation model, we must first choose adequate values for the numbers of discrete scatterers  $N_{1,1}$ ,  $N_{1,2}$ , and  $N_{1,3}$ . Based on our own simulation experiences and suggested by [35], a reasonable values can be 40, which can be considered as a good trade-off between realization complexity and accuracy. To simulate rigorous channels, e.g., very high VTD, the number of effective scatterers can be increased to improve the performance of the channel simulator. In addition, when  $\beta_T^{(n1)} = \beta_R^{(n2)} = \beta_R^{(n3)} = 0^\circ$ , the proposed 3D model will be reduced to a 2D two-ring and multiple ellipses model. The impact of elevation angle has been evaluated in [10] by comparing between the 3D and 2D models in terms of narrowband statistical properties.

Fig. 5 shows the simulation results compared with the measurement results in [24]. As the local SI is time-variant value, by using the proper channel model parameters, the simulation mean result can fit the measured results, i.e., the 1479 ms and 1412 ms for scenarios 2 and 3, respectively. Furthermore, the complementary cumulative distribution function (CCDF) of the SRL are compared in Fig. 6. Observing from Figs. 5, the mean value of simulated results can match the measured results very well. Both the measured and simulation results in Figs. 5 and 6 demonstrate that low VTD channels have longer SI when the Tx and Rx moving in the same direction. So that the proposed 3D wideband non-WSS V2V channel model has the ability to capture the channel non-stationarity when the Tx and Rx are driving in the same direction.

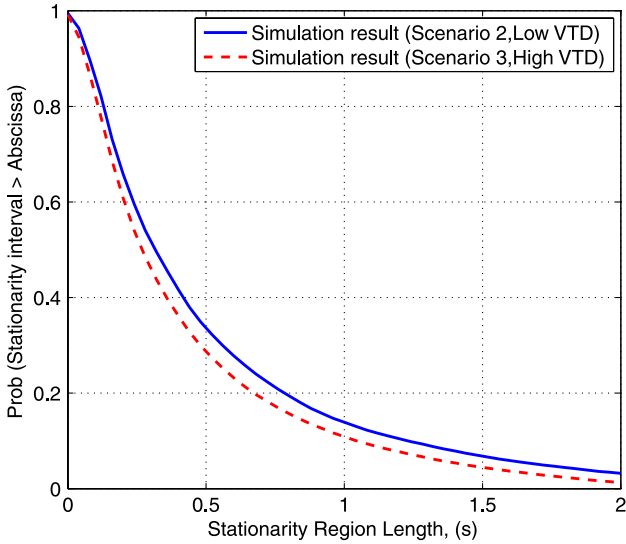


Fig. 6. Simulated CCDF of the stationary interval for different VTDs.

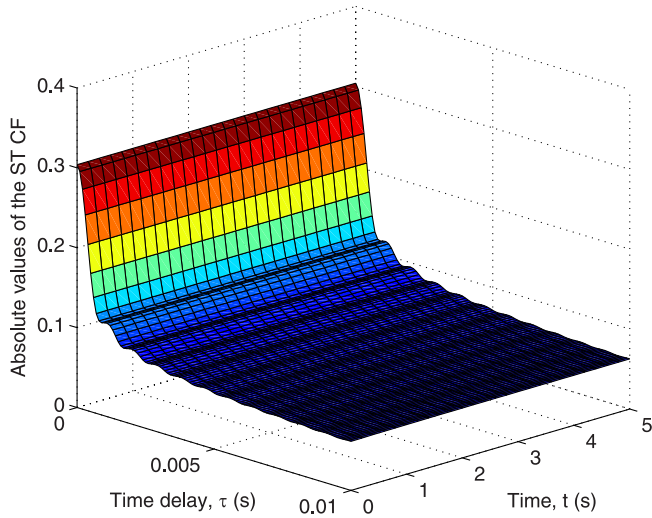


Fig. 7. The absolute values of the local ST CF for the 3D reference model at tap 1 in the high VTD scenario ( $\delta_T = \delta_R = 3\lambda$ ,  $\beta_{T0}^{(1)} = 6.7^\circ$ ,  $\beta_{R0}^{(2)} = 17.2^\circ$ ,  $\beta_{R0}^{(3)} = 31.6^\circ$ ).

### B. Local ST CF

Fig. 7 depict the absolute value of 3D local ST CFs when  $\delta_T = \delta_R = 3\lambda$  for tap 1 at high VTD. Fig. 8 shows the absolute value of the local ST CF for the 3D reference model, simulation model, and simulated result in different VTD scenarios. Observing from Fig. 8, the 3D reference model, simulation model, and simulated result of tap 1 at low VTD  $t = 0$  s closely match to each other, which indicates the correctness of our derivations. Therefore, we only show the simulation results of the rest curves for clarity purpose. It is obvious that the VTD greatly affects the ST CF at different taps. In low VTD scenario, the local ST CF is always higher than that in high VTD scenario. In others words, the local ST CF in high VTD is fading faster than that in low VTD scenario. For further comparison along different time slots, i.e.,  $t = 0$  s and 2 s, the variations of local ST CFs for low and high VTDs at the first tap and second tap are indiscernible. This is due to the

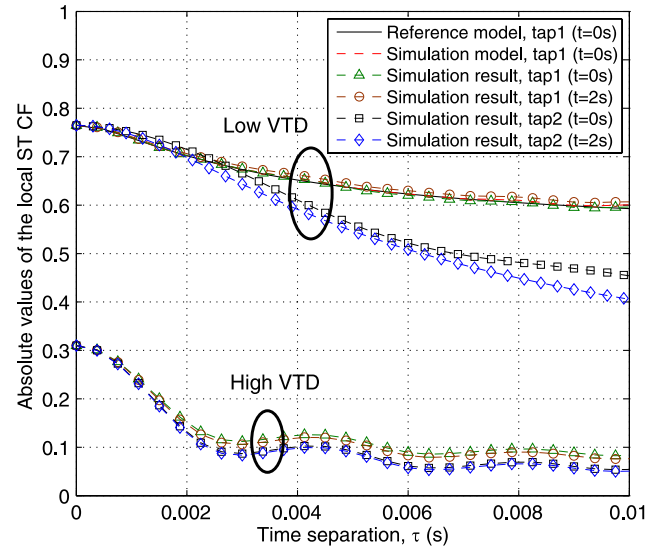


Fig. 8. The absolute values of the local ST CF for the 3D reference model, simulation model, and simulated results in different VTD scenarios ( $\delta_T = \delta_R = 3\lambda$ ,  $\beta_{T0}^{(1)} = 6.7^\circ$ ,  $\beta_{R0}^{(2)} = 17.2^\circ$ ,  $\beta_{R0}^{(3)} = 31.6^\circ$ ).

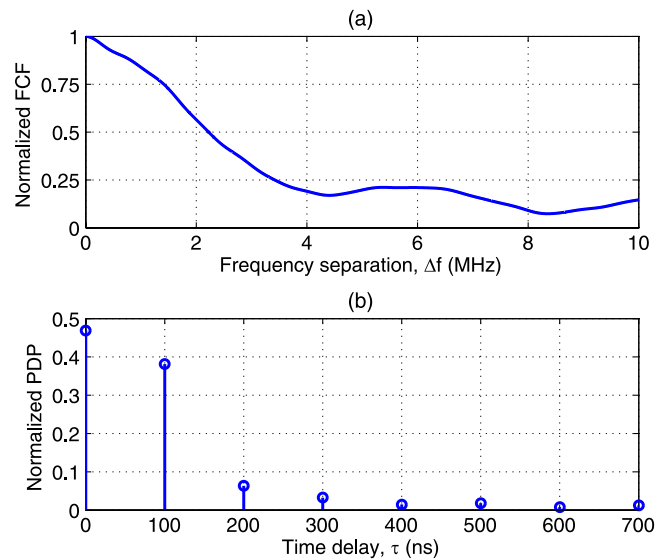


Fig. 9. The absolute value of the (a) FCF and (b) PDP for the 3D V2V channel models.

assumption of the same moving direction and velocity of the Tx and Rx, which are relatively stationary. In fact, the non-stationarity of the local ST CF is caused only by the single-bounced component resulting from the elliptic-cylinder model, which describes the roadside stationary scatterers that have the relative movement in reference to the Tx or Rx. Nevertheless, it is necessary to extend our 3D non-WSS model to support the V2V channel of opposite motion in the future work. The challenge in this future work is that three different locations between the Tx and Rx have to be distinguished, i.e., vehicles are approaching, passing, and leaving.

### C. Local FCF and PDP

Fig. 9(a) and (b) show the local FCF and corresponding PDP of the proposed models, respectively. The results are obtained

by using the following parameters reported in [32], i.e., the propagation delays  $\{\tau'_l\}_{l=1}^8 = \{0, 100, 200, 300, 400, 500, 600, 700\}$  ns and the tap powers  $\{c_l^2\}_{l=1}^8 = \{-10.3, -11.2, -19, -21.9, -25.3, -24.4, -28.0, -26.1\}$  dB when the Tx and Rx are moving in the same direction. In Fig. 9(b), note that the normalized PDP uses fractional values converted from “dB,” which aims to normalize the summation of all tap powers to 1. Again, it is obvious that the local FCF and the PDP are completely determined by the number of propagation paths  $L$  (i.e., taps), the path gains  $c_l$ , and the propagation delays  $\tau'_l$ . Once we have the measured local FCF and PDP at different time slots, we can easily fit the proposed model to measurement data.

## VI. CONCLUSION

In this paper, we have proposed a non-WSS 3D theoretical RS-GBSM and corresponding SoS simulation model for non-isotropic scattering wideband MIMO V2V Ricean fading channels. The 3D parameter computation method, named as MEV, has been used to jointly calculate the azimuth and elevation angles for the simulation model. Based on the proposed channel models, important local statistical properties have been derived and thoroughly investigated, i.e., local ST CF, local FCF, and PDP. The proposed 3D reference and simulation models have been verified by simulated results indicating the correctness of our derivations and simulations.

In addition, the non-stationarity of the proposed channel models has been verified by measurements in terms of local SI. By comparing these results, we can conclude that the VTD has major impact on these local statistical properties. The numerical and simulations results have clearly shown that the low VTD always results in better channel conditions than the high VTD case. Consequently, the proposed models have the ability to investigate the impact of the VTD on channel statistics and capture the non-stationarity of V2V channels when the Tx and Rx are moving in the same direction.

## REFERENCES

- [1] H. Hartenstein and K. P. Laberteaux, “A tutorial survey on vehicular ad hoc networks,” *IEEE Commun. Mag.*, vol. 46, no. 6, pp. 164–171, Jun. 2008.
- [2] W. Chen and S. Cai, “Ad hoc peer-to-peer network architecture for vehicle safety communications,” *IEEE Commun. Mag.*, vol. 43, no. 4, pp. 100–107, Apr. 2005.
- [3] C.-X. Wang *et al.*, “Cooperative MIMO channel models: A survey,” *IEEE Commun. Mag.*, vol. 48, no. 2, pp. 80–87, Feb. 2010.
- [4] X. Cheng *et al.*, “Cooperative MIMO channel modeling and multi-link spatial correlation properties,” *IEEE J. Sel. Areas Commun.*, vol. 30, no. 2, pp. 388–396, Feb. 2012.
- [5] *Standard for Wireless Local Area Networks Providing Wireless Communications While in Vehicular Environment*, IEEE Std P802.11p/D2.01, Mar. 2007.
- [6] C.-X. Wang, X. Cheng, and D. I. Laurenson, “Vehicle-to-vehicle channel modeling and measurements: Recent advances and future challenges,” *IEEE Commun. Mag.*, vol. 47, no. 11, pp. 96–103, Nov. 2009.
- [7] X. Cheng *et al.*, “Wideband channel modeling and ICI cancellation for vehicle-to-vehicle communication systems,” *IEEE J. Sel. Areas Commun.*, vol. 31, no. 9, pp. 434–448, Sep. 2013.
- [8] X. Cheng, C.-X. Wang, B. Ai, and H. Aggoune, “Envelope level crossing rate and average fade duration of non-isotropic vehicle-to-vehicle Ricean fading channels,” *IEEE Trans. Intell. Transp. Syst.*, vol. 15, no. 1, pp. 62–72, Feb. 2014.
- [9] G. Bakhshi, R. Saadat, and K. Shahtalebi, “Modeling and simulation of MIMO mobile-to-mobile wireless fading channels,” *Int. J. Antennas Propag.*, vol. 2012, Mar. 2012, Art. ID. 846 153.
- [10] Y. Yuan, C.-X. Wang, X. Cheng, B. Ai, and D. I. Laurenson, “Novel 3D geometry-based stochastic models for non-isotropic MIMO vehicle-to-vehicle channels,” *IEEE Trans. Wireless Commun.*, vol. 14, no. 1, pp. 298–309, Jan. 2014.
- [11] I. Sen and D. W. Matolak, “Vehicle-vehicle channel models for the 5-GHz band,” *IEEE Trans. Intell. Transp. Syst.*, vol. 9, no. 2, pp. 235–245, Jun. 2008.
- [12] X. Cheng, C.-X. Wang, D. I. Laurenson, S. Salous, and A. V. Vasilakos, “New deterministic and stochastic simulation models for non-isotropic scattering mobile-to-mobile Rayleigh fading channels,” *Wireless Commun. Mobile Comput.*, vol. 11, no. 7, pp. 829–842, Jul. 2011.
- [13] A. S. Akki and F. Haber, “A statistical model for mobile-to-mobile land communication channel,” *IEEE Trans. Veh. Technol.*, vol. 35, no. 1, pp. 2–10, Feb. 1986.
- [14] A. S. Akki, “Statistical properties of mobile-to-mobile land communication channels,” *IEEE Trans. Veh. Technol.*, vol. 43, no. 4, pp. 826–831, Nov. 1994.
- [15] A. G. Zajić and G. L. Stüber, “Space-time correlated mobile-to-mobile channels: Modelling and simulation,” *IEEE Trans. Veh. Technol.*, vol. 57, no. 2, pp. 715–726, Mar. 2008.
- [16] X. Cheng, C.-X. Wang, D. I. Laurenson, S. Salous, and A. V. Vasilakos, “An adaptive geometry-based stochastic model for non-isotropic MIMO mobile-to-mobile channels,” *IEEE Trans. Wireless Commun.*, vol. 8, no. 9, pp. 4824–4835, Sep. 2009.
- [17] X. Cheng, C.-X. Wang, Y. Yuan, D. I. Laurenson, and X. Ge, “A novel three-dimensional regular-shaped geometry-based stochastic model for MIMO mobile-to-mobile Ricean fading channels,” in *Proc. IEEE VTC-Fall*, Ottawa, ON, Canada, Sep. 2010, pp. 1–5.
- [18] A. G. Zajić and G. L. Stüber, “Three-dimensional modeling, simulation, and capacity analysis of space-time correlated mobile-to-mobile channels,” *IEEE Trans. Veh. Technol.*, vol. 57, no. 4, pp. 2042–2054, Jul. 2008.
- [19] A. G. Zajić and G. L. Stüber, “Three-dimensional modeling and simulation of wideband MIMO mobile-to-mobile channels,” *IEEE Trans. Wireless Commun.*, vol. 8, no. 3, pp. 1260–1275, Mar. 2009.
- [20] P. T. Samarasinghe, T. A. Lamahewa, T. D. Abhayapala, and R. A. Kennedy, “3D mobile-to-mobile wireless channel model,” in *Proc. IEEE AusCTW*, Canberra, ACT, Australia, Feb. 2010, pp. 30–34.
- [21] T.-M. Wu and T.-H. Tsai, “Novel 3-D mobile-to-mobile wideband channel model,” in *Proc. IEEE APSURSI*, Chungli, Taiwan, Jul. 2010, pp. 1–4.
- [22] J. Karedal *et al.*, “A geometry-based stochastic MIMO model for vehicle-to-vehicle communications,” *IEEE Trans. Wireless Commun.*, vol. 8, no. 7, pp. 3646–3657, Jul. 2009.
- [23] M. Boban, T. T. V. Vinhoza, M. Ferreira, J. Barros, and O. K. Tonguz, “Impact of vehicles as obstacles in vehicular ad hoc networks,” *IEEE J. Sel. Areas Commun.*, vol. 29, no. 1, pp. 15–28, Jan. 2011.
- [24] A. Paier *et al.*, “Non-WSSUS vehicular channel characterization in highway and urban scenarios at 5.2 GHz using the local scattering function,” in *Proc. IEEE Int. ITG WSA*, Vienna, Austria, Feb. 2008, pp. 9–15.
- [25] O. Renaudin, V.-M. Kolmonen, P. Vainikainen, and C. Oestges, “Car-to-car channel models based on wideband MIMO measurements at 5.3 GHz,” in *Proc. EuCAP*, Berlin, Germany, Mar. 2009, pp. 635–639.
- [26] O. Renaudin, V.-M. Kolmonen, P. Vainikainen, and C. Oestges, “Non-stationary narrowband MIMO inter-vehicle channel characterization in the 5-GHz band,” *IEEE Trans. Veh. Technol.*, vol. 59, no. 4, pp. 2007–2015, May, 2010.
- [27] O. Renaudin, V.-M. Kolmonen, P. Vainikainen, and C. Oestges, “Wideband measurement-based modeling of inter-vehicle channels in the 5 GHz band,” *IEEE Trans. Veh. Technol.*, vol. 62, no. 8, pp. 3531–3540, Oct. 2013.
- [28] A. Chelli and M. Patzold, “A non-stationary MIMO vehicle-to-vehicle channel model based on the geometrical T-junction model,” in *Proc. IEEE WCSP*, Nanjing, China, Nov. 2009, pp. 1–5.
- [29] A. Chelli and M. Patzold, “A non-stationary MIMO vehicle-to-vehicle channel model derived from the geometrical street model,” in *Proc. IEEE VTC-Fall*, San Francisco, CA, USA, Sep. 2011, pp. 1–6.
- [30] U. A. K. C. Okonkwo, S. Z. M. Hashim, R. Ngah, N. F. Nanyan, and T. Abd Rahman, “Time-scale domain characterization of nonstationary wideband vehicle-to-vehicle propagation channel,” in *Proc. IEEE APACE*, Port Dickson, Malaysia, Nov. 2010, pp. 1–6.
- [31] J. Maurer, T. Fugen, M. Porebska, T. Zwick, and W. Wisebeck, “A ray-optical channel model for mobile to mobile communications,” presented at the COST 2100/4th MCM, Wroclaw, Poland, Feb. 2008, Paper TD(08)430.

- [32] G. Acosta and M. A. Ingram, "Six time- and frequency-selective empirical channel models for vehicular wireless LANs," *IEEE Veh. Technol. Mag.*, vol. 2, no. 4, pp. 4–11, Dec. 2007.
- [33] G. Matz, "On non-WSSUS wireless fading channels," *IEEE Trans. Wireless Commun.*, vol. 4, pp. 2465–2478, Sep. 2005.
- [34] K. V. Mardia and P. E. Jupp, *Directional Statistics*. Chichester, U.K.: Wiley, 2000.
- [35] M. Pätzold, *Mobile Radio Channels*, 2nd ed. Chichester, U.K.: Wiley, 2012.
- [36] T. Zwick, C. Fischer, D. Didascalou, and W. Wiesbeck, "A stochastic spatial channel model based on wave-propagation modeling," *IEEE J. Sel. Areas Commun.*, vol. 18, no. 1, pp. 6–15, Jan. 2000.
- [37] E. A. Jorswieck and H. Boche, "Multiple-antenna capacity in the low-power regime: Channel knowledge and correlation," in *Proc. IEEE ICASSP*, Philadelphia, PA, USA, Mar. 2005, pp. 385–388.
- [38] A. L. Moustakas, S. H. Simon, and A. M. Sengupta, "MIMO capacity through correlated channels in the presence of correlated interferers and noise: A (not so) large N analysis," *IEEE Trans. Inf. Theory*, vol. 49, no. 10, pp. 2545–2561, Oct. 2003.
- [39] M. Chiani, M. Z. Win, and H. Shin, "MIMO networks: The effects of interference," *IEEE Trans. Inf. Theory*, vol. 56, no. 1, pp. 336–349, Jan. 2010.
- [40] E. Gschwendtner and W. Wiesbeck, "Ultra-broadband car antennas for communications and navigation applications," *IEEE Trans. Antennas Propag.*, vol. 51, no. 8, pp. 2020–2027, Aug. 2003.



**Yi Yuan** received the B.Sc. degree (with distinction) in electronic engineering from Tianjin University of Technology, Tianjin, China, in 2006, the M.Sc. degree (with distinction) in mobile communications from Heriot-Watt University, Edinburgh, U.K., in 2009, and the joint Ph.D. degree from The University of Edinburgh and Heriot-Watt University, Edinburgh, U.K., in 2014. He has been with Ocado Technology, U.K., as a Wireless Engineer-Specialist/R&D, since 2014. His main research interests include industrial wireless control systems, wireless network optimization, mobile-to-mobile communications and advanced wireless MIMO channel modeling and simulation.



**Cheng-Xiang Wang** (S'01–M'05–SM'08) received the B.Sc. and M.Eng. degrees in communication and information systems from Shandong University, Jinan, China, in 1997 and 2000, respectively, and the Ph.D. degree in Wireless Communications from Aalborg University, Aalborg, Denmark, in 2004.

He has been with Heriot-Watt University, Edinburgh, U.K., since 2005 and was promoted to Professor in 2011. He is also an Honorary Fellow of the University of Edinburgh, U.K., and a Chair/Guest Professor at Shandong University and Southeast

University, China. He was a Research Fellow at the University of Agder, Grimstad, Norway, from 2001–2005, a Visiting Researcher at Siemens AG-Mobile Phones, Munich, Germany, in 2004, and a Research Assistant at Technical University of Hamburg-Harburg, Hamburg, Germany, from 2000–2001. His current research interests include wireless channel modeling and simulation, green communications, cognitive radio networks, vehicular communication networks, massive MIMO, millimetre wave communications, and 5G wireless communications. He has edited one book and published one book chapter and over 210 papers in refereed journals and conference proceedings.

Prof. Wang served or is currently serving as an editor for 8 international journals, including IEEE TRANSACTIONS ON VEHICULAR TECHNOLOGY (2011–) and IEEE TRANSACTIONS ON WIRELESS COMMUNICATIONS (2007–2009). He was the leading Guest Editor for IEEE JOURNAL ON SELECTED AREAS IN COMMUNICATIONS, Special Issue on Vehicular Communications and Networks. He served or is serving as a TPC member, TPC Chair, and General Chair for over 70 international conferences. He received the Best Paper Awards from IEEE Globecom 2010, IEEE ICCT 2011, ITST 2012, and IEEE VTC 2013-Fall. He is a Fellow of the IET, a Fellow of the HEA, and a member of EPSRC Peer Review College.



**Yejun He** (SM'09) received the B.S. degree from Huazhong University of Science and Technology, Wuhan, China, in 1994, the M.S. degree in communication and information system from Wuhan University of Technology (WHUT), Wuhan, China, in 2002, and the Ph.D. degree in information and communication engineering from Huazhong University of Science and Technology (HUST) in 2005.

From September 2005 to March 2006, he was a Research Associate with the Department of Electronic and Information Engineering, The Hong Kong

Polytechnic University. From April 2006 to March 2007, he was a Research Associate with the Department of Electronic Engineering, Faculty of Engineering, The Chinese University of Hong Kong. From July 2012 to August 2012, he was a Visiting Professor with the Department of Electrical and Computer Engineering, University of Waterloo, Waterloo, ON, Canada. From October 2013 to October 2015, he is an Advanced Visiting Scholar (Visiting Professor) with School of Electrical and Computer Engineering, Georgia Institute of Technology, Atlanta, Georgia, USA. He is currently a Full Professor at Shenzhen University, China. His research interests include channel coding and modulation; MIMO-OFDM wireless communication; space-time processing; smart antennas and so on. He is a senior member of the China Institute of Communications and China Institute of Electronics. He has served as associate editor of the *Security and Communication Networks* journal since 2012. He is the principal investigator for more than 10 current or finished research projects including NSFC, the integration project of production teaching and research by Guangdong Province and Ministry of Education as well as the Science and Technology Program of Shenzhen City and so on. He has authored or co-authored more than 80 research papers as well as applied for 12 patents.



**Mohammed M. Alwakeel** was born in Tabuk, Saudi Arabia, in 1970. He received the B.S. degree in computer engineering and the M.S. degree in electrical engineering, both from King Saud University, Riyadh, Saudi Arabia, in 1993 and 1998, respectively, and the Ph.D. degree in electrical engineering from Florida Atlantic University, Boca Raton, FL, USA, in 2005. From 1994 to 1998, he was a Communications Network Manager at The National Information Center, Saudi Arabia. From 1999 to 2001, he was with King Abdulaziz University. From

2009 to 2010, he was an Associated Professor and the Dean of Computers and Information Technology College, University of Tabuk. He is now The Vice Rector of University of Tabuk for Development and Quality. His current research interests include teletraffic analysis, mobile satellite communications, sensor networks, and cellular systems.



**el-Hadi M. Aggoune** (M'83–SM'93) received the M.S. and Ph.D. degrees in electrical engineering from the University of Washington (UW), Seattle, WA, USA. Currently, he is a Professor and Director of the Sensor Networks and Cellular Systems (SNCS) Research Center, University of Tabuk, Tabuk, Saudi Arabia. He has taught graduate and undergraduate courses in electrical engineering at a number of universities in the US and abroad. He served at many academic ranks including Endowed Chair Professor and Vice President and Provost. He

is listed as Inventor in a major patent assigned to the Boeing Company. His research work is referred to in many patents including patents assigned to ABB, Switzerland and EPRI, USA. His research interests include modeling and simulation of large scale networks, sensors and sensor networks, scientific visualization, and control and energy systems. He was the winner of the Boeing Supplier Excellence Award. He was also the winner of the IEEE Professor of the Year Award, UW Branch. He has authored many papers in IEEE and other journals and conferences. He is serving on many technical committees. He is a Professional Engineer registered in the State of Washington.